LAWRENCE
LIVERMORE
NATIONAL
LABORATORY

UCRL-JRNL-220707

An Analysis of the X-Ray Diffraction Signal for the (alpha) - (epsilon) Transition in Shock-Compressed Iron: Simulation and Experiment

J. Hawreliak, J. D. Colvin, D. H. Kalantar, H. E. Lorenzana, J. S. Stolken, H. M. Davies, T. C. Germann, B. L. Holian, K. Kadau, P. S. Lomdahl, A. Higginbotham, K. Rosolankova, J. Sheppard, J. S. Wark

April 19, 2006

Physical Review B

An Analysis of the X-Ray Diffraction Signal for the $\alpha - \epsilon$ Transition in Shock-Compressed Iron: Simulation and Experiment

J. Hawreliak,* J.D. Colvin, D.H. Kalantar, H.E. Lorenzana, and J.S. Stölken

Lawrence Livermore National Laboratory, Livermore CA 94550

H.M. Davies

AWE Aldermaston, Reading, United Kingdom

T.C. Germann, B.L. Holian, K. Kadau, and P.S. Lomdahl

Los Alamos National Laboratory, Los Alamos, New Mexico 87545

A. Higginbotham, K. Rosolankova, J. Sheppard, and J.S. Wark

University of Oxford, Oxford, United Kingdom

(Dated: April 7, 2006)

Abstract

Recent published work has shown that the phase change of shock compressed iron along the [001] direction does transform to the ϵ (HCP) phase similar to the case for static measurements. This article provides an indepth analysis of the experiment and NEMD simulations, using x-ray diffraction in both cases to study the crystal structure upon transition. Both simulation and experiment are consistent with a compression and shuffle mechanism responsible for the phase change from BCC to HCP. Also both show a polycrystalline structure upon the phase transition, due to the four degenerate directions the phase change can occur on, with grain sizes measured of 4nm in the NEMD simulations and $\approx$ 2nm in the experiment. And looking at the time scale of the transition the NEMD shows the transition from the compressed BCC to HCP is less then 1.2 ps where the experimental data places an upper limit on the transition of 80 ps.

PACS numbers:

*Electronic address: hawreliak1@llnl.gov

I. INTRODUCTION

It is almost a full century since the start of the Nobel-prize-winning work of Bridgman showing that many crystals transform to new structures under the influence of static pressure [1]. There is also a large body of evidence that many pressure-induced phase transitions occur under shock-compression, which is remarkable considering that under such conditions the time-scale over which the pressure is applied to the material is many orders of magnitude shorter than in the static experiments. The most well known, and indeed most widely-studied of these shock-induced transformations is the $\alpha - \epsilon$ transition in iron, where the original body-centred-cubic (bcc) lattice is thought to transform to hexagonal close-packed (hcp). The significance of this transition in iron is related to the millennia-old importance of iron in the development of human civilization, as well as in geophysics, being the principal element within the earth's core. It is even speculated that the crystalline properties of the earth's core have measurable affects at the surface [2]. However, despite having been studied for several decades, until recently, no direct experimental data about how the atoms can rearrange on such ultrafast timescales existed.[3, 4].

The first tentative evidence for this transition under shock conditions came half a century ago, when J.M. Walsh reported data on the propagation of high-pressure shock waves in Armco iron[5] that were in disagreement with an extrapolation of Bridgman's original static compressibility measurements [6] : Walsh's measurements implied a compression up to 20% higher then Bridgman's data. This discrepancy was explained by Bancroft, Peterson, and Minshall, whose work indicated the existence of a multiple-wave shock structure within a single sample [7, 8]. They associated the splitting of the waves with elastic-plastic response and the subsequent transformation of the iron to a different phase. Analysis of the wave profiles implied that the onset of the phase transition occurred at a pressure of 130 kbar. At that time the $\alpha - \epsilon$ (i.e. bcc - hcp) phase transition in iron was unknown, and it was speculated that the infered transition could be the $\alpha - \gamma$ phase transition (bcc-fcc) which was known to occur at $\approx$1000 K at standard pressure (see Fig. 1). Initial electrical resistivity tests under static pressure were inconclusive in confirming phase transition at 130 kbar, and as a result the validity of Minshall's data was called into question. Much of the criticism directed towards the then newly-emerging field of shock physics was no doubt due in part to the difficulty in believing that a solid-solid phase transition could occur on a microsecond

time scale [9].

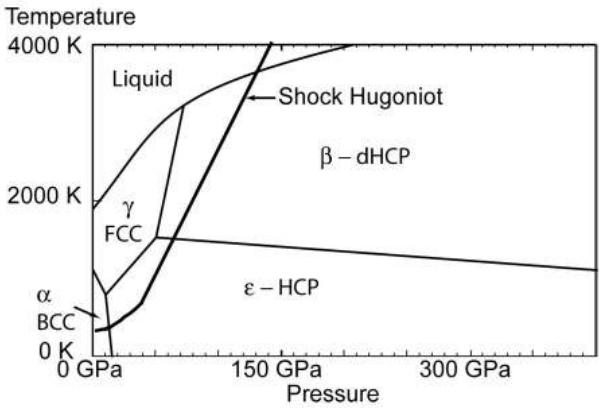

FIG. 1: The known phase diagram of iron under static conditions, from Saxena and Dubrovinsky [10], with the shock hugoniot overlaid [11, 12]

It was only several years after Minshall's shock-wave work that the crystallographic evidence for a bcc-hcp transition at 130 kbar was obtained in static X-ray diffraction experiments by Jamieson and Lawson [13]. This confirmation that a phase transition occurred under static conditions at an (almost) identical pressure to that deduced from the earlier shock-wave measurements countered the doubts about shock wave techniques. This discovery of one of the most important phase transitions known to man has long been hailed as one of the major triumphs of the field of shock-wave physics. It has been assumed ever since that the transition associated with the multiple-waves seen in shock experiments, and that observed under static high-pressure conditions, are one and the same transition.

However, there was no direct evidence that the new wave profiles which appear in the shock data seen at pressures which correspond to the phase change seen in static experiments are the same. In particular the shear stress experienced by crystals under the two different techniques can be radically different: in static measurements the crystals are compressed under hydrostatic conditions, with no intentionally imposed shear. On the other hand, in planar shock wave experiments the crystal sample is subjected to uniaxial strain and hydrostatic conditions are approached only if significant plastic flow occurs (driven by the high shear stress) before the transition pressure is achieved, or if significant shear stress is relieved during the transition itself. Even then the material will retain some degree of strength with some residual shear stress remaining. Thus on ultra-fast time-scales of a shock,

before significant plastic flow may have had time to occur, there may be very significant differences between the conditions experienced by a shocked sample and hydrostatically compressed sample, and these differences may well alter not only the path taken to the new phase, but perhaps even the phase itself.

There is a long history of using X-ray diffraction techniques to study and identify the phase diagrams of materials subjected to static compression [14, 15]. For the case of iron, after the initial identification of the bcc-hcp phase by Jamieson and Lawson [13], Mao and co-workers made first determined the lattice parameters of the bcc and hcp phases as a function of static pressure up to 30 GPa [16]. Since that time numerous X-ray diffraction and X-ray absorption fine structure (XAFS) studies of the transition under static compression have been undertaken [16–19]. Furthermore, an analysis of the observed c/a ratios has led to suggestions as to the specific path by which the transition takes place – an important subject which we discuss later in this paper for the case of shock compressed samples.

In contrast to static techniques, until very recently no direct structural information on the shock-induced transition in iron had been presented – it had simply been assumed that the phase transition at 130 kbar, inferred from wave profiles, was the bcc-hcp transition. Under this assumption the transition time can be inferred from the rise-time of the appropriate wave. Transformation times of less than 50 – 100 nsec have been deduced by this technique[20–23] . It has been suspected that the residual microstructure left after the passage of the shock can be used to put an upper limit on the transition time, and using this method, timescales below 5 nsec have been suggested. Evidence for an even more rapid timescale has come from the irradiation of polycrystalline iron with laser pulses as short as 120 fs. After such irradiation, the ϵ phase has been detected in a quenched form within the sample by use of electron diffraction [24], although whether this transition was shock or thermally induced is difficult to say.

Given both the historical and scientific importance of the $\alpha - \epsilon$ transition, *in situ* determination of the structure during shock compression is clearly of importance, and it is in this context that the recent direct confirmation of the shock induced phase transformation by use of both nanosecond EXAFS, [4] and x-ray diffraction [3] should be viewed. In the work using nanosecond X-ray diffraction discussed here, we showed conclusively that under laser-shock compression, iron transforms to the hcp phase, with the transition taking place on the timescale of the experiment.

This paper puts forward a fuller analysis of the experimental data and simulation than could be presented in Kalantar et al. [3]. In particular, we provide a more detailed comparison of the experimental data with multi-million atom non-equilibrium molecular dynamics (NEMD) simulations, [25], and will show that the lack of plasticity before the onset of the transition, polycrystalline structure and orientation seen in those simulations is also a salient feature within the data. The molecular dynamics simulations also gives insight into the possible mechanism by which the transition proceeds. This mechanism is consistent with the experimental data . We compared simulated diffraction patterns with the experimental data showing how they differ for various proposed transition paths, illustrating which path offers best agreement with the experimental patterns.

The paper is arranged in the following manner. We first describe the possible mechanisms that have previously been suggested for the $\alpha - \epsilon$ transition in iron under static compression, and discuss how these mechanisms may be modified under conditions of unaixial strain with no plasticity. We then present a post-processed analysis of the NEMD simulations of the shock-induced phase transition, and present simulated diffraction patterns. These simulated diffraction images, along with the direct information about atomic positions within the simulation, point to a particular mechanism for the transition under shock compression that differs from the suggested pathway under static compression [17]. We then present the experimental data showing how detailed fitting of simulated diffraction lines to the data restricts the possible paths by which the transition occurred. Finally, we discuss similarities between the NEMD simulations and the experimental data – in particular the apparent lack of plasticity before the onset of the transition, the information that can be gleaned from the diffraction data on the size of the 'grains' produced during the transition, and the limits that can now be placed in the ultimate timescale of the transition under shock loading.

II. TRANSITION MECHANISMS UNDER HYDROSTATIC COMPRESSION

The kinematics of the iron $\alpha - \epsilon$ phase transition under hydrostatic compression has been described by Wang and Ingalls [17] . They put forward three different possible mechanisms for the transition and discuss the consistency of each model with EXAFS measurements taken under hydrostatic pressures between 50 kbar and 180 kbar. We summarise these three mechanisms in the next two sections: Mechanism I and Mechanism II+IIa (two of

the mechanisms described by Wang and Ingalls are combined into a single section because it would be impossible to distinguish the two processes by their end states using x-ray diffraction). After this discussion of the proposed physics under hydrostatic conditions, in a further section we then turn our attention to possible modifications to the mechanisms for the case where pressure is applied to the sample by shock loading.

A. Mechanism I

The first proposed mechanism for the phase transition is a two step process. The initial step involves the atoms in the $(110)_{\mathrm{BCC}}$ plane being compressed along the $[001]_{\mathrm{BCC}}$ axis and expanding along $[\bar{1}10]_{\mathrm{BCC}}$ to form a hexagon, as shown in Fig. 2. The second step is a shuffle of alternate $(110)_{\mathrm{BCC}}$ planes in the $[1\bar{1}0]_{\mathrm{BCC}}$ direction to create the two atom primitive cell. By this means the resulting HCP structure has hexagonal planes – the $(0002)_{\mathrm{HCP}}$ planes – corresponding to what were (110) planes in the BCC phase. The c-axis in the HCP phase, i.e. the [0002] direction, corresponds to the $[\bar{1}\bar{1}0]_{\mathrm{BCC}}$ direction. Similarly we find the $[10\bar{1}0]_{\mathrm{HCP}}$ axis aligned with the original $[001]_{\mathrm{BCC}}$ axis, $[0002]_{\mathrm{HCP}} \parallel [110]_{\mathrm{BCC}}$ and $(2\bar{1}\bar{1}0)_{\mathrm{HCP}} \parallel (002)_{\mathrm{BCC}}$. These relations are those originally put forward in 1934 by Burgers. [26]

Figure 2 is a schematic diagram of the atomic motion leading to the phase change showing (a) the initial positions of the atoms in the $(110)_{\mathrm{BCC}}$ plane and arrows indicating the motion due to compression/expansion and (b) the final positions of the atoms as a hexagon in the $(0002)_{\mathrm{HCP}}$ plane as well as arrows showing the direction of shuffle. The filled and hollow circles denote atoms in different original $(110)_{\mathrm{BCC}}$ planes. Figure 2 also shows an important consequence of the shuffling of alternate $(110)_{\mathrm{BCC}}$ planes when using x-ray diffraction to determine the crystal structure. The shift causes a change in the stacking of the $(\bar{1}12)_{\mathrm{BCC}}$ planes such that in the HCP phase these planes have effectively been doubled in period. Thus diffraction from the $(\bar{1}100)_{\mathrm{HCP}}$ plane would not be seen from a corresponding plane in BCC, as it would correspond to Miller indices of $(\frac{\bar{1}}{2}\frac{1}{2}1)_{\mathrm{BCC}}$. Period doubling (due to the change from a monatomic to diatomic primitive cell) is one of the hallmarks of the transition to the HCP phase, and thus the $(\bar{1}100)_{\mathrm{HCP}}$ plane is one of the diffraction planes used in diagnosing the existence of the new phase.

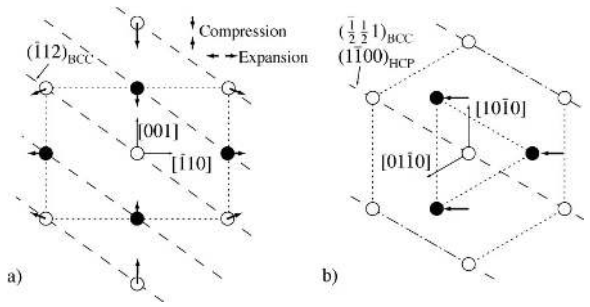

FIG. 2: Schematic diagram showing atomic motion corresponding to Mechanism I. The $(110)_{\mathrm{BCC}}$ and $(0002)_{\mathrm{HCP}}$ planes are in the plane of the paper, where the hollow and solid circles denote atoms in the page and above the page respectively. The arrows denote the direction ofmotion of the atoms. a) shows the initial atomic locations with the arrows showing the motion due to the expansion/compression. b) shows the final HCP state of the atoms with arrows showing the direction of the shuffle. a) defines the coordinate system in terms of the BCC indices and shows the location of the $(\bar{1}12)_{\mathrm{BCC}}$ planes b) defines the coordinate system for the HCP with the $(1\bar{1}00)_{\mathrm{HCP}}$ planes labelled.

B. Mechanisms II + IIa

The other two models for the transition put forward by Wang and Ingalls are also multi-step processes: Mechanism II is once more a two-step process, whereas Mechanism IIa is a three-step process. However, both the initial step and the final structure are the same for the two models, which is why we treat them here within the same section. The initial step of both mechanisms is responsible for the motion of atoms within a BCC plane into a hexagonal arrangement, with once more the subsequent steps effectively resulting in the shuffle, and thus period doubling. However, the first step for these two models is quite different to that proposed in Mechanism I, as can be seen in Figure 3, resulting in a different orientation of the final HCP unit cell with respect to the initial BCC unit cell than found in Mechanism I, which can be distinguished by x-ray diffraction.

Figure 3 shows a schematic diagram of the formation of the hexagon in both Mechanisms II and IIa. This initial step is a shear motion, such that the atoms in the $(\bar{1}12)_{\mathrm{BCC}}$ planes move in the $[\bar{1}1\bar{1}]_{\mathrm{BCC}}$ direction at the same time as there is compression in the $[1\bar{1}\bar{2}]_{\mathrm{BCC}}$ direction. These two components of atomic motion – that along $[\bar{1}1\bar{1}]_{\mathrm{BCC}}$, and that along $[1\bar{1}\bar{2}]_{\mathrm{BCC}}$, are shown in Figure 3. We relate the motion along $[\bar{1}1\bar{1}]_{\mathrm{BCC}}$ to an angle θ, which

is related to the final angle between the initial BCC state and the final HCP state. The motion along $[1\bar{1}\bar{2}]_{\mathrm{BCC}}$ by a compression,Δ. In Fig. 3 the first arrow by the hollow atoms denotes the motion due to the shear and the second due to the compression.

The hexagons formed by the shear and compression described above are slightly rotated about their c-axes – i.e. about $[0002]_{\mathrm{HCP}}/[110]_{\mathrm{BCC}}$: for the case of hydrostatic compression it can be shown that to form hexagons in this manner the hexagon is rotated by $\theta = 5.3^{\circ}$ or equivelantly the $(2\bar{1}\bar{1}0)_{\mathrm{HCP}}$ plane will be at a 5.3° angle with respect to the original $(002)_{\mathrm{BCC}}$. In addition, the overall compression is 8%. This is an important point to which we shall return when discussing analogous mechanisms for the transition under conditions of uniaxial shock compression, this will also address the factor g in Fig. 3 which is 1 for the hydrostatic case.

Once the hexagons have been formed alternate planes must now shuffle to provide the period doubling. For Mechanism II this step is similar to the shuffle which occurs in Mechanism I, i.e. alternate $(110)_{\mathrm{BCC}}$ planes shift, thus generating the final HCP structure. Figure 3 simple shows the resultant of the two step process for the solid atoms.

On the other hand the period-doubling process corresponding to Mechanism IIa is different. In this case it is proposed that the final HCP phase is reached by motion of the atoms that takes the crystal through a meta-stable face-centred-cubic (FCC) phase, and a further step is required to take it to the HCP phase. It is proposed that the FCC phase is reached by a shearing of the $(110)_{\mathrm{BCC}}$ planes in the $[0\bar{1}10]_{\mathrm{HCP}}$ direction. Subsequently, in the third step, the slip of pairs of $(110)_{\mathrm{BCC}}$ type planes occurs in the $[01\bar{1}0]_{\mathrm{HCP}}$ direction. For both mechanisms, the final state is an HCP structure where the $[10\bar{1}0]_{\mathrm{HCP}}$ direction is rotated 5.3°from the original $[001]_{\mathrm{BCC}}$ direction about the $[110]_{\mathrm{BCC}}$ or $[0002]_{\mathrm{HCP}}$ axis, which can not be differentiated using x-ray diffraction.

Wang and Ingalls state that Mechanism IIa is preferred under hydrostatic conditions because the energetics are more favorable for the series of shear and slip systems, as opposed to a shuffle of alternate planes. In addition they argue that temperature dependent effects suggest a meta-stable FCC phase, and furthermore passing through the FCC phase will generate a c/a ratio of 1.633 at the threshold for transition, as observed in their experiments. As stated in the introduction the forces exerted on the sample in the hydrostatic and shock systems are completely different, and this will have consequences on the mechanics of the phase transition. We will now alter each of these mechanisms, constraining them to con-

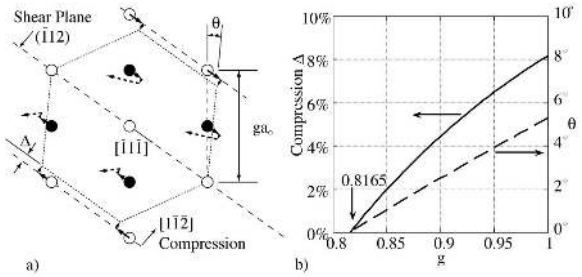

FIG. 3: Schematic diagram showing the formation of the hexagon in both Mechanisms II and IIa. (a) The $(110)_{\mathrm{BCC}}$ plane with the atoms in their initial positions. The $(\bar{1}12)_{\mathrm{BCC}}$ shear plane, the $[\bar{1}1\bar{1}]_{\mathrm{BCC}}$ direction, and the $[1\bar{1}\bar{2}]_{\mathrm{BCC}}$ direction are labeled. The solid arrows denote the direction of the atomic motion due to the shear/compression, i.e. the motion along the $[\bar{1}1\bar{1}]_{\mathrm{BCC}}$ direction and $[1\bar{1}\bar{2}]_{\mathrm{BCC}}$ direction respectively. The dashed arrows represent the effective overall movement of the atoms when the crystal structure undergoes period doubling, beit via Mechanism II or IIa. In the case of shock compression along $[001]_{\mathrm{BCC}}$, we assume the BCC lattice is elastically compressed, so the lattice parameter along $[001]_{\mathrm{BCC}}$ have a length ga_0, where $g <= 1$ before the shear occurs. (b) As described in the text, the resultant rotation of the HCP unit cell, θ, and required compression along $[1\bar{1}\bar{2}]_{\mathrm{BCC}}$ to form the hexagon in the initial step, are both functions of g, where $g = 1$ for hydrostatic conditions.

ditions seen in the experimental data, i.e. an initial uni-axial compression and no plastic dilatation.

III. PHASE TRANSITION UNDER UNIAXIAL SHOCK COMPRESSION ALONG [001]

In both the Molecular Dynamics (MD) simulations and experiments described in the later sections of this paper the $\alpha - \epsilon$ transition was observed in single crystal iron samples shocked along the [001] direction. In order to discuss the possible mechanism that we might invoke by which the transition occurred, and then to compare this mechanism with the hydrostatic case, it is first necessary to consider what is thought to happen to the lattice of shocked crystals in the absence of phase transitions.

The response of a crystal to uniaxial shock compression is a function of the peak stress imposed. Below a certain threshold stress, known as the Hugoniot Elastic Limit (HEL), the

material responds in an elastic and reversible manner, without the generation of any defects or dislocations: no plastic flow occurs. Thus below the HEL, for a single crystal shocked along a principal axis, we can think of each the atoms within the sample as simply moving closer to one another along the shock propagation direction. In particular for the case here, where the crystal is shocked along [001], each of the cubic unit cells will become tetragonal (though we shall refer to them as BCC cells compressed along [001]).

For shock pressures above the HEL it is known that plastic flow occurs. Initially, as the pressure is increased above the HEL, we find the velocity of the plastic wave is lower than that of the elastic wave, and thus a two-wave structure is formed.As the velocity of the plastic wave increases with shock compression, above a critical compression the plastic wave has a velocity equal or surpassing that of the elastic wave, and a single wave is observed: this is known as the strong shock regime.

The precise mechanisms by which plasticity occurs – i.e. the detailed physics of the generation and propagation of dislocations, and the relevant time-scales, are still a matter of considerable debate. As an example there is excellent evidence that in FCC materials, such as Copper, plastic flow under shock compression occurs on timescales less than a nansecond (as evinced by experiment)[27]. MD simulations suggest the timescales are actually much shorter for such materials – perhaps a few tens of picoseconds [28]. That said, little experimental or MD work has yet been performed on the elastic plastic transition in BCC materials.

It is within this context that no (or at least very little) evidence for the onset of plasticity for BCC iron, both in the MD simulations that we show in section IV,[25] and in the experiment described in section V,[3].That is to say, although the Iron was compressed far above what (on much longer time-scales) is normally considered to be the HEL, no plastic flow occurred. We will return to the evidence for this statement in the sections IV and V.

The implication of this lack of plasticity, when combined with the imposed condition of uniaxial strain, is that the mean spacing between the atoms in the direction orthogonal to the shock front cannot change. How such lack of plasticity impacts on the proposed mechanics of the transition is addressed in the following sections. A prime symbol is added to each mechanism to denote that atomic motion is similar to the hydrostatic mechanism (which are not primed) but with the added constraints of an initial uni-axial compression and no plastic deformation, i.e. starting the transformation from an initial state where $g < 1$.

A. Mechanism I′

Under uni-axial strain conditions within the shock propagating along the $[001]_{\mathrm{BCC}}$ direction, the analogue to Mechanism I (hydrostatic mechanism) will again be a compression of the atoms in the $(110)_{\mathrm{BCC}}$ plane along the $[001]_{\mathrm{BCC}}$ direction. Unlike the hydrostatic case, Mechanism I′ will have no expansion of the lattice in the $[\bar{1}10]_{\mathrm{BCC}}$ direction. Thus we require that the hexagon in the $(110)_{\mathrm{BCC}}$ plane must be generated simply by compression along $[001]_{\mathrm{BCC}}$ – this fixes the total compression to 18.3% with respect to the uncompressed BCC state. The second step of Mechanism I′ is the same as its hyrdostatic counter part with alternate $(110)_{\mathrm{BCC}}$ planes shuffle in the $[\bar{1}10]_{\mathrm{BCC}}$ direction by $a_o/(3\sqrt{2})$ The resulting structure has a c/a ratio of $\sqrt{3}$ for when a hexagon is formed in the $(110)_{\mathrm{BCC}}$ planes. Clearly, under further shock compression, it is possible to further compress the crystal, which will result in a distorted HCP structure.

B. Mechanism II′+IIa′

When considering the analogues of the hydrostatic mechanisms Mechanisms II and IIa we note that Mechanism II′ and IIa′ under uniaxial shock compression along the $[001]_{\mathrm{BCC}}$ direction we expect the crystal to be in a uniaxially compressed BCC state before the atoms in the $(110)_{\mathrm{BCC}}$ plane move to form a hexagon. The shear rotation angle, θ, and compression along the $[1\bar{1}\bar{2}]_{\mathrm{BCC}}$ direction, Δ, for Mechanism II′ and IIa′ will thus be a function of the degree of shock compression before this initial stage in the transformation, g. This relationship is plotted in Fig. 3. In this figure, g is related to the degree of shock compression before the hexagon forms – that is to say $g = 1$ corresponds to the case where the lattice is initially uncompressed, similar to the hydrostatic case, where as $g = 0.8165$ corresponds to the case where the BCC lattice is compressed by 18.3% – i.e. is exactly the same as Mechanism I′, where no rotation of the lattice is required to produce a hexagon. With no initial compression of the BCC cells the rotation of the HCP unit cell around $[0002]_{\mathrm{HCP}}$ is 5.3°and the c/a ratio is 1.63 as before for Mechanisms II and IIa. For 6% pre-compression Mechanism II′ and IIa′ suggest a rotation is 3.6°, with a c/a ratio of 1.67 and at 18.3% pre-compression there is, as noted above, no rotation and a c/a ratio of $\sqrt{3}$ as already state this is Mechanism I′ .

C. Degeneracy

In describing the possible mechanisms by which the $\alpha - \epsilon$ transition might occur, we have hitherto been referring to motion of atoms along a specific set of planes, and specific directions. There is clearly some degeneracy – that is to say there is more than one equivalent plane, and/or direction, in which the atoms can move. However, not all families of planes are equivalent. We thus state here the degeneracies that are present within the problem for the potential mechanisms under shock compression.

Using Mechanism I′, as an example, once lattice has been compressed by 18.3% along the $[001]_{\mathrm{BCC}}$ direction the atoms will form hexagons in the $\{110\}_{\mathrm{BCC}}$ family of planes. This means there are four degenerate directions the $\{110\}_{\mathrm{BCC}}$ planes can shift to cause the period doubling. Shuffling along the $[1\bar{1}0]_{\mathrm{BCC}}$ and $[\bar{1}10]_{\mathrm{BCC}}$ directions will generate and HCP structure with the c-axis parallel to the $[110]_{\mathrm{BCC}}$ direction. The x-ray diffraction signal generated by both shifts will be identical because the $c - axis$ is in the same direction. Alternatively, shuffling along the $[110]_{\mathrm{BCC}}$ and $[\bar{1}\bar{1}0]_{\mathrm{BCC}}$ directions will generate an HCP structure with the c-axis parallel to the $[1\bar{1}0]_{\mathrm{BCC}}$ direction. Again, the x-ray diffraction signal generated by both shifts will be identical because the c-axis is in the same direction, but the x-ray diffraction will be different then the case for the $[1\bar{1}0]_{\mathrm{BCC}}$ or $[\bar{1}10]_{\mathrm{BCC}}$ shuffles. These two possible orientations of the HCP lattice with respect to the BCC lattice are shown in Figure 5. In the first case, (a), we have assumed that the shuffle of the atoms is along $[\bar{1}10]_{\mathrm{BCC}}$, the c-axis is out of the plane of the page (i.e. along $[110]_{\mathrm{BCC}}$), and the HCP planes that correspond to what were the $(\bar{1}12)_{\mathrm{BCC}}$ planes have doubled in period, to become the $(1\bar{1}00)_{\mathrm{HCP}}$ planes. Note, however, that what were the $(112)_{\mathrm{BCC}}$ planes (not shown) have not doubled in period. In contrast, in (b) we show the corresponding position of the atoms for the same original BCC cell if, after forming the hexagon, the shuffle of the atoms is out of the plane of the page, along the $[110]_{\mathrm{BCC}}$ direction. In this case the c-axis of the hexagon is in the plane of the paper – labelled $[0001]_{\mathrm{HCP}}$. Now what were the $(\bar{1}12)_{\mathrm{BCC}}$ planes have not doubled in period, and in the HCP system are labelled $(2\bar{1}\bar{1}2)_{\mathrm{HCP}}$.

Importantly, as these two sets of planes and shuffle directions are fully degenerate, we expect that under shock conditions, if Mechanism I′ is operating, a single crystal of iron transforming to HCP will contain equal numbers of these two types of 'grains', with one grain type with the c-axes aligned along the original $[110]_{\mathrm{BCC}}$ and $[1\bar{1}0]_{\mathrm{BCC}}$ direction.

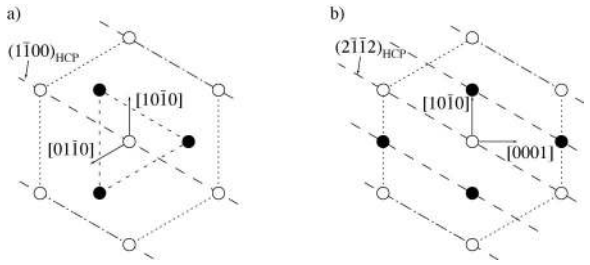

FIG. 4: Two different views of the period doubling in he HCP lattice. a) shows the planes parallel to the (110) planes associated with the shift, and the spacing of the $(1\bar{1}00)_{\rm HCP}$ plane is twice that of the $(\bar{1}12)_{\rm BCC}$. b) shows the case when the shift is into/out of the page, the spacing of the $(2\bar{1}\bar{1}2)$ planes is that same as the compressed $(\bar{1}12)_{\rm BCC}$. These different lattice orientations can be resolved by x-ray diffraction.

Similar degeneracies are clearly also present within Mechanisms II′ and IIa′. There are two possible orientations for the c-axis of the HCP lattice as for Mechanism I′, and, for each of these orientations, the shuffle of alternate planes of atoms could occur in the positive or negative sense. However, there is a further degeneracy in Mechanisms II′ and IIa′ in that the rotation of the hexagon around its c-axis could be in either the clockwise or anti-clockwise sense due to a shear along the $[\bar{1}1\bar{1}]$ or $[1\bar{1}\bar{1}]$ directions respectively . Thus if the lattice transformed by Mechanisms II′ or IIa′, there are 4 possible orientations of the hexagon with respect to the original BCC lattice.

D. The $\alpha - \epsilon$ phase transition in the reciprocal lattice

X-ray diffraction has been proven as an excellent diagnostic in determining the crystal structure of a material. We will show in section IV that we can use a simulated x-ray diffraction diagnostic to study the molecular dynamic simulations as well. To understand how to compare the reciprocal lattice to the x-ray diffraction data we look at the transformation of the reciprocal lattice in a similar way as we did the physical space lattice in the previous section.

Figure 5 a) shows the reciprocal lattice of a perfect BCC lattice, with several points labeled. Note the line denoting the length of the $(\bar{1}12)$ reciprocal lattice vector. In Fig. 5 b) we show the reciprocal lattice for a perfect HCP crystal in the same plane, where we have assumed that the c-axis of the HCP lattice is out of the plane of the paper, which is the

$[2\bar{1}\bar{1}0]$x$[0\bar{1}10]$ plane. For those points labelled with two sets of Miller indices, it is the upper set that correspond to a crystal in the stated orientation, i.e. with the [0002] direction out of the page. Note the period doubling in what was the $[\bar{1}12]$ direction. As noted previously, there is an equal possibility that in the transformed crystal has a c-axis in the plane of the paper. If this were the case, the eight lattice points enclosed by dashed circles would not be present in this plane – indeed the reciprocal lattice in this plane would be identical to the reciprocal lattice of the BCC crystal, and the lower set of Miller indices would be the appropriate labelling of the points with respect the HCP cell (note the c-axis, [0002], now in the plane of the paper). The HCP reciprocal lattice points which correspond directly with a BCC reciprocal lattice point have two HCP labels as these points will exist in both HCP orientations.

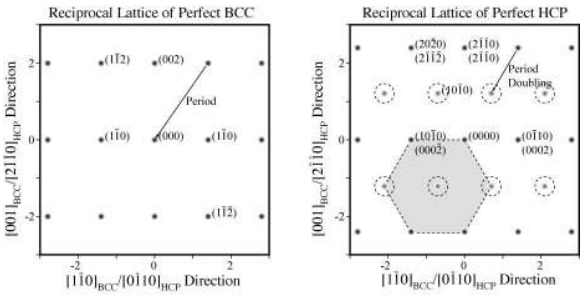

FIG. 5: The reciprocal lattice of a) BCC and b) HCP. a) The reciprocal lattice of a BCC in the (110) plane. This plane shows the points which fall on opposing corners and the one in the middle of the top and bottom faces. Some points have been labeled with their associated diffraction plane to provide an orientation. b) The HCP reciprocal lattice showing the hexagonal base and the possible labels depending on the orientation of the HCP. For both plots the dimensions of k-space are in units of $2\pi/a_0$, where a_0 is the lattice constant of the BCC unit cell.

As we shall see in the sections that follow, these concepts are important in understanding the diffracted signal observed in the experiments, and in the processing and interpretation of the molecular dynamics simulations.

IV. IRON NEMD CALCULATIONS

A. Description of the Simulations

Having considered possible mechanisms by which iron may rapidly transform from a BCC to HCP structure under shock conditions we now turn our attention to large-scale Non-Equilibrium molecular dynamic (NEMD) simulations of this transformation. Such NEMD simulations of single crystals of iron uniaxially shocked along the $[001]_{\mathrm{BCC}}$ direction have been performed by Kadau and co-workers [25]. The simulations were generated using a massively parallel MD code "SPaSM" ("Scalable Parallel Short-range Molecular Dynamics") [29], running on a 12-processor shared-memory Sun Enterprise 4000. Each simulation modeled 7.84×10^6 atoms in samples 57.4 nm long in the shock direction ($[001]_{\mathrm{BCC}}$) and 40.2 nm in both the lateral directions ($140\times140\times200$ BCC unit cells).

The shock was generated using the momentum mirror method [30]. Atoms were specularly reflected by an infinitely massive, perfectly flat piston moving at velocity u_p, generating a shock wave moving at velocity u_s. Periodic boundary conditions were applied in the lateral directions ($[100]_{\mathrm{BCC}}$ and $[010]_{\mathrm{BCC}}$). The duration of each simulation was <10 ps, approximately the time taken for the shock to transit the sample. Interactions between the atoms were modeled by use of the Voter-Chen EAM Fe potential [31]. This potential predicts the $\alpha-\epsilon$ transition under shock compression at a pressure of just over 15 GPa, in reasonable agreement with experimentally measured threshold pressures of $\sim$13 GPa [7, 32].

Four simulations are studied with increasing piston velocities (u_p) as follows:**A** 362 ms^{-1}, **B** 471 ms^{-1},**C** 689 ms^{-1}, and **D** 1087 ms^{-1}, as shown in Fig. 6,. These velocities correspond to pressures along the shock propagation direction of 15.0 GPa, 19.6 GPa, 28.7 GPa, and 52.9 GPa, respectively. In Fig. 6 the atoms are color coordinated according to the number of nearest neighbours within a radius of 2.75Å, such that unshocked BCC appears grey, uniaxially compressed BCC appears dark grey, and HCP appears light grey (note that full color images of this figure can be found in the original paper, ref. [25]).

B. Simulated X-ray Diffraction from NEMD Simulations

The NEMD calculations provide the coordinates of the iron atoms as a function of time as the shock propagates through the sample. Whilst there are several ways of analysing

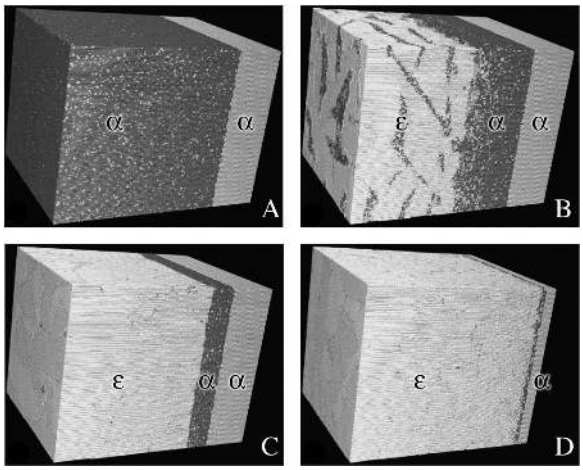

FIG. 6: Pictorial representations of four MD simulation where the color coding corresponds to the number of nearest neighbours within a radius of 2.75Å. Grey is uncompressed BCC, dark grey is uniaxially compressed BCC and light grey is HCP. The labels on the images correspond to the phase in that region.[25]

this data to obtain information about the mechanism by which the calculations predict the phase transition occurs, we choose to analyse the data in Fourier space, as this provides a direct correspondence with the experimental X-ray diffraction patterns discussed in following sections. Thus, in order to generate simulated diffraction patterns we take the atomic data in real space, and generate a map in reciprocal space simply by taking a 3D Fourier transform of the atomic positions [33, 34].

$$F(\vec{k}) = |\sum_{j=1}^{N} e^{i\vec{k}\cdot\vec{r}_j}|^2 \tag{1}$$

where N is the number of atoms and $\vec{r}_j$ is the location of the j^{th} atom. Whilst a simple transform of this type ignores the finite size of the atom (the atomic form factor), this could, if need be, be included by convolving the transform of the form factor with that of the lattice. However, the effect of this is merely to reduce the intensity of the scattering for high Miller indices. We have ignored this effect in this analysis.

As described in the previous section, it is expected that the HCP phase is formed by the $(110)_{\text{BCC}}$ or $(\bar{1}10)_{\text{BCC}}$ planes of the BCC lattice forming hexagons, either by direct compression down the $[001]_{\text{BCC}}$ direction as in Mechanism I′, or by a combination of rotation and compression, as in Mechanisms II′ and IIa′. Thus we consider slices in Fourier space through the $(110)_{\text{BCC}}$ plane of the crystal, with orthogonal axes along the $[100]_{\text{BCC}}$ and

$[1\bar{1}0]_{\mathrm{BCC}}$ BCC directions.

The atomic coordinates for the four simulations shown in Fig. 6 were post-processed using Eq. 1 to generate simulated X-ray diffraction patterns. As described in section III D the diffraction planes will become points in reciprocal lattice space, refer to Fig. 5 to provide an orientation. The results of the $[1\bar{1}0]_{\mathrm{BCC}} \times [001]_{\mathrm{BCC}}$ plane are shown in Fig. 7. The calculated diffraction from simulation **A** shows only the BCC structure, i.e. a rectangular structure with peaks that correspond to the corners and the center of the face of a cube. However, each original lattice peak is now split in two representing diffraction from both shocked and unshocked portions of the crystal in the simulation. The unshocked part of the crystal gives rise to the perfect BCC diffraction peaks, whereas the compressed crystal gives rise to peaks corresponding to a reciprocal lattice slightly expanded along $[001]_{\mathrm{BCC}}$. We note that there is no shift of the diffraction spots in the $[1\bar{1}0]_{\mathrm{BCC}}$ direction, confirming that the simulated shocked crystal is elastically compressed. Compression of the lattice in real space causes an expansion of the reciprocal lattice along the shock direction. Measuring the location of the reciprocal lattice points we find that the real lattice has been compressed by 7.0±0.5% uni-axial compression for this simulation.

As can be seen from Fig. 6, all three of the simulations **B, C, and D** have pressures that exceed the exceed the threshold for the phase transition. This is reflected in the reciprocal lattices seen in Fig. 7. We observe that each of the reciprocal lattice points that was present in the original BCC crystal and that had a non-zero component along $[001]_{\mathrm{BCC}}$, are now split into three distinct spots, corresponding to diffraction from the unshocked BCC lattice, the compressed BCC lattice, and a diffuse peak at an even higher compression. In addition Fig. 7 **B,C, and D** show diffraction spots, in dashed circles, in positions that create a hexagonal pattern in this plane which is what we would expect for an HCP lattice. These are due to the period doubling of the $(1\bar{1}2)_{\mathrm{BCC}}$ planes. These new spots are not split, but are single spots, as they only occur above the threshold pressure when the additional diffuse peak is observed on the original BCC peaks. The structure of these diffuse points shows that the simulations has under gone a phase change at these pressures and the structure is consistent with HCP iron.

The relative intensity of the individual split spots (such as the $(002)_{\mathrm{BCC}}$ – $(2\bar{1}\bar{1}0)_{\mathrm{HCP}}$ spot) varies, as one might expect, according to the relative volume of material in the corresponding state. That is to say, for simulation **B**, about one half of the crystal is in the HCP phase,

with the other half of the crystal almost equally divided between unshocked and shocked BCC material. On the other hand, for simulation **D** the diffraction from the HCP phase dominates the diffraction.

Analysis of the positions of the diffraction spots in reciprocal lattice space corresponding to the uniaxially compressed BCC lattice indicates that, as seen in simulation **A**, the crystal in this region reaches a maximum compression of 7.0±0.5% for all of the simulations. On the other hand, the peak corresponding to the HCP crystal shows that the movement of the atoms which form the $(002)_{\mathrm{BCC}}$ stacking compressed along the $[001]_{\mathrm{BCC}}$ direction by 11.5±0.5%, 13.8±0.5%, and 17.4±0.5% for simulations **B,C, and D** respectively upon transition to the HCP phase. This compressions, deduced from the shift of the spots in reciprocal space, agree with the direct density measurements from the MD simulations, Fig. 8.The NEMD simulations show that with only compression in the shock direction ($[001]_{\mathrm{BCC}}$) only the highest compression of 52.9 GPa generates a structure which approaches an ideal hexagonal structure in the $(110)_{\mathrm{BCC}}$ plane (i.e. approaching 18.3% compression) creating an HCP with two a-axes of the same length and a c/a ratio of $\sqrt{3}$. As well as looking at the reciprocal lattice in the $(110)_{\mathrm{BCC}}$ plane, we also calculated the pattern in the $(\bar{1}10)_{\mathrm{BCC}}$ plane – the plane normal to the ones shown in Fig. 7 (i.e. the $[001]_{\mathrm{BCC}}[110]_{\mathrm{BCC}}$ reciprocal lattice plane). We find the identical pattern, suggesting that both orientations of the c-axis of the HCP are present in the NEMD simulation, i.e. there are components of the crystal which have the c-axis parallel to $[110]_{\mathrm{BCC}}$ and others which are parallel to $[1\bar{1}0]_{\mathrm{BCC}}$.

On the time scale of the simulations there is no plastic flow in the NEMD simulated crystal. Plastic flow, by the generation and motion of dislocations, would result in a reduction in the mean lattice parameter perpendicular to the shock propagation direction, and thus, in reciprocal space, an expansion of the lattice. It is evident from all four plots that no perpendicular expansion is observed on these timescales for either the compressed BCC or HCP material. Figures 9 and 10 shows an expanded view of the $(1\bar{1}2)$ point in reciprocal lattice space. This illustrates that there is very little lateral shift of the peaks in reciprocal space, i.e. no motion in real space. The 19.6 GPa case shows no lateral deformation of the compressed BCC peak, i.e. no plastic deformation occured before the phase change, and a shift of the HCP peak corresponding to 0.7% of the transformed HCP lattice perpendicular to the shock when fitting a Gaussian distribution to the broad peak. Fitting the HCP peak when the compression is increased to 52.9 GPa suggests that there is a 0.7% lateral com-

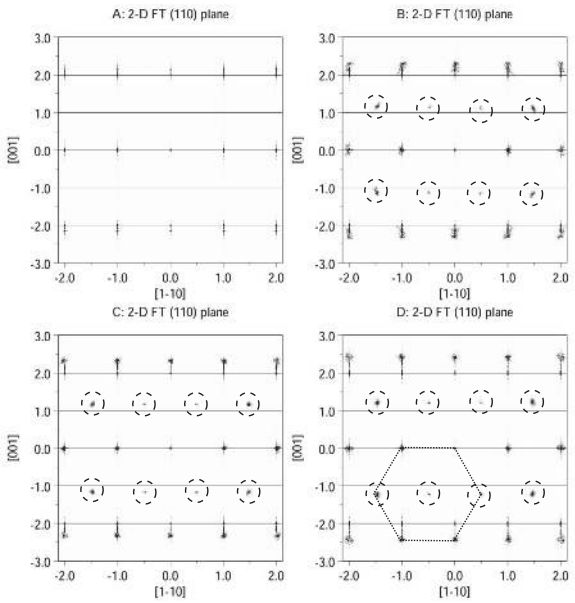

FIG. 7: The $[001]_{BCC}$x$[110]_{BCC}$ plane for the four MD simulations. Simulation **A** shows only the expansion of the BCC lattice along the shock direction. **B,C, and D** show the formation of the HCP structure, for 15 GPa, 19.6 GPa, 28.7 GPa, and 52.9 GPa respectively.

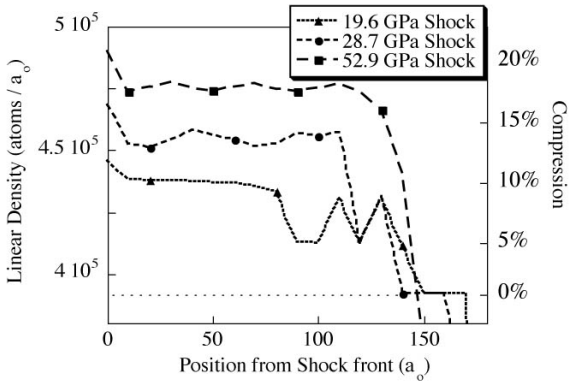

FIG. 8: The linear density in the simulations plotted as function of position, showing compression that agrees with the simulated diffraction. There is an initial compression of ≈7% of the iron BCC lattice followed by a larger compression upon phase change to HCP.

pression of the atoms in the HCP phase. Note for this simulation that the small number atoms in the uni-axially compressed BCC region and static BCC region cause the peak to severely broaden along the $[001]_{BCC}$ direction. The lack of plastic deformation is consistent with the fact that the large number of dislocations required for plastic relaxation are not

observable in the real space images of the NEMD simulation shown in Fig. 6.

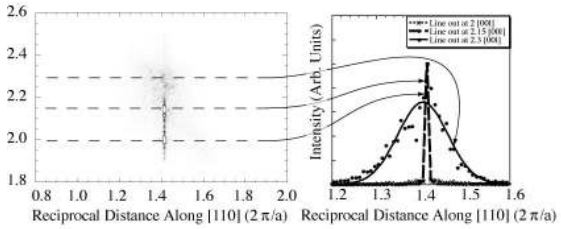

FIG. 9: Close up of the $(112)_{\mathrm{BCC}}$ point in reciprocal space sectioned through the [001]x[110] plane for the 19.6 GPa compression. The lineouts show a more detailed location of the points along the $[110]_{\mathrm{BCC}}$ axis. There is a shift of the broad HCP peak suggesting a 0.7% lateral expansion

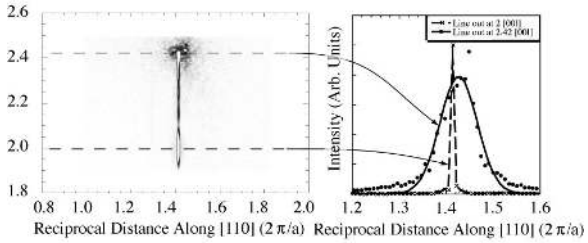

FIG. 10: Close up of the $(112)_{\mathrm{BCC}}$ point in reciprocal space sectioned through the [001]x[110] plane for the 52.9 GPa compression. The lineouts show a more detailed location of the points along the $[110]_{\mathrm{BCC}}$ axis. There is a shift of the broad HCP peak suggesting a 0.7% lateral compression

C. Possible mechanisms for the phase change

As described in section III two different mechanisms were proposed by Wang and Ingalls as possible mechanisms for the $\alpha - \epsilon$ phase change in iron under hydrostatic conditions, and we described these mechanisms under constraints particular to shock compression. We could differentiate between the two types – Mechanism I′ versus Mechanism II′ and IIa′ based on whether there was a rotation of the HCP lattice with respect to the BCC lattice (i.e. an angle between the $(002)_{\mathrm{BCC}}$ and $(2\bar{1}\bar{1}0)_{\mathrm{HCP}}$ planes). For the hydrostatic case, Mechanism II′ and IIa′ we would expect a rotation of the HCP lattice of order 5.3°. This might legitimately be taken as the upper bound estimate of the rotation observed if the

preferred pathway is Mechanism II′ or IIa′, as it requires no pre-compression of the BCC lattice by the shock. The MD simulations predict a compression wave propagating through the BCC crystal, compressing it by 7%, before the transformation to an HCP-like structure. From Fig. 3 , we see that for a perfect hexagon to be formed following the initial uniaxial compression a rotation on the order 3.5°would still occur. With no mean motion of the atoms transverse to the shock, a compression of 18.3% is required to obtain a perfect hexagon whatever the mechanism. However, the MD shows transformation to an HCP-like structure at compressions somewhat below this value. Nevertheless, if Mechanisms II′ or IIa′ are possible candidates, there should be some rotation of the lattice with respect to the original BCC lattice.

A rotation in real space is evident in reciprocal space as a similar rotation in the intensity peaks. In Fig. 11 we show an expanded view of the $(2\bar{1}\bar{1}0)_{\mathrm{HCP}}/(002)_{\mathrm{BCC}}$ spot in reciprocal space. Also shown on the plot are dashed lines that run through the origin in reciprocal space, but make angles of ±2°and ±5°relative to the [001] axis. Since there are two possible directions that the rotation can occur we would expect to see the HCP feature composed of two spots, each slightly shifted off the axis. However, the spot still appears to be a single diffuse spot although somewhat broad (of order ±1°FWHM). This suggests that the $\alpha - \epsilon$ transition occurs by Mechanism I′ in the NEMD simulations.

A similar conclusion is reached by an analysis of the positions of the atoms in the NEMD simulation in real space. We have performed an analysis whereby for every atom in the simulations in the HCP phase we search for the position of the closest neighbouring atom in approximately the [001] direction. A histogram of the angle between these pairs of atoms is plotted in Fig. 12. Along with the shock compressed simulation the angle between pairs of atoms in an unshocked compressed HCP sample at 500K is plotted to show the angular broadening is consistent with relative thermal fluctuations. This distribution peaks on the $[001]_{\mathrm{BCC}}$ axis indicating no overall lattice rotation. Again the lack of rotation of the lattice suggest that mechanism I is the pathway for the transition.

V. EXPERIMENTAL SETUP

The experiments were performed using the OMEGA [15], Janus, and Vulcan [16] lasers. Samples of 200 - 270 μm thick single crystal [001] iron with a purity of 99.94 % from

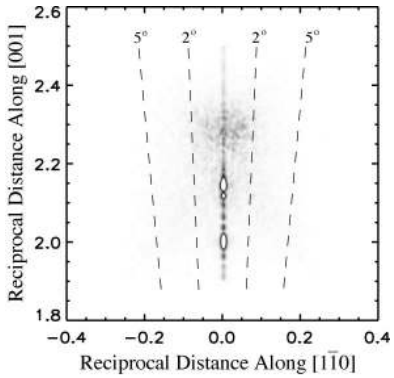

FIG. 11: A close up of the $(002)_{\mathrm{BCC}}/(2\bar{1}\bar{1}0)_{\mathrm{HCP}}$ diffraction plane in reciprocal lattice space in the [110] plane. Angular contours are overlaid on to illustrate the effect of overall lattice rotation. The single diffuse spot $(2\bar{1}\bar{1}0)_{\mathrm{HCP}}$ is consistent with no rotation of the lattice.

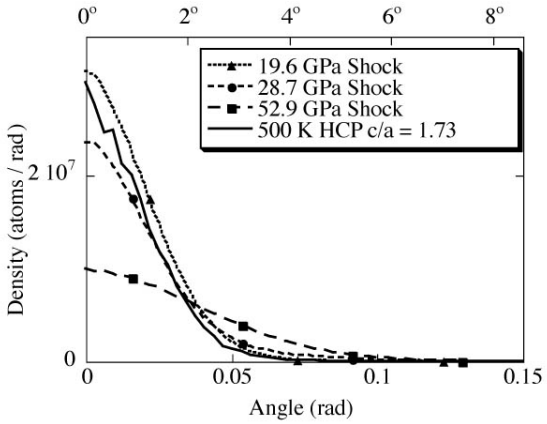

FIG. 12: Plot of the relative orientation of adjacent atoms relative to the shocked axis. The peak at 0 suggests that there is no rotation upon phase change in the simulation and the broadening is consistent with thermal broadening as shown by the plotting of a 500K perfect HCP crystal.

Accumet Materials were coated with a 16–20 μm parylene-N ablator layer followed by a 0.1μm aluminum shine-through layer. These samples were shock loaded by direct laser irradiation at 2×10^{10} to 1×10^{12} Wcm^{-2} using 2–6 ns constant intensity laser pulses. The diameter of the crystal shocked by the laser was determined by the laser focal spot size, and was of order 2-3 mm.

The shocked iron crystals were interrogated by wide-angle in situ diffraction, which has been described extensively elsewhere [35–37]. In this technique, a transient source of iron K-shell X-rays is created with another laser beam, or set of laser beams, synchronous to

the shock-driving beams. These beams are focussed onto a metal foil in a small laser spot, heating the foil to a high temperature, to create a plasma with a high population of He-like ions, with strong emission from the resonance lines of the ions. This creates a 100μm $\rightarrow$ 200μm diameter source of divergent x-rays that diffract from the surface of the crystal, and were recorded on a wide angle detector. In these experiments, iron K-shell x rays with a wavelength of 1.85Åwere created by direct irradiation of an iron foil positioned 1.3 mm from the shocked crystal sample. The duration of the X-ray pulses closely followed that of the 2-4 ns laser pulse that created them [38]. For the 200 μm thick iron samples referred to above, the X-rays were diffracted from the shocked-side of the iron crystal in reflection geometry – which we refer to as Bragg geometry. Additional experiments were conducted using 10 μm thick single crystal samples of iron. For these thinner samples it was also possible to perform diffraction in transmission geometry, which we refer to as Laue geometry. Due to the divergence of the X-rays, and the large angle which the crystal subtends to the X-ray source, the x rays are diffracted from many different lattice planes in the crystal, resulting in multiple line features on the detector. Two wide angle multiple film packs (MFPs) covering a total of nearly 2π steradians recorded the diffracted signal in both Bragg and Laue geometry, as shown in Fig. 13. Compression of the lattice by the shock results in the Bragg diffraction condition being met at a different angle and location on the crystal, leading to shifts in the lines recorded radiation on the detector.

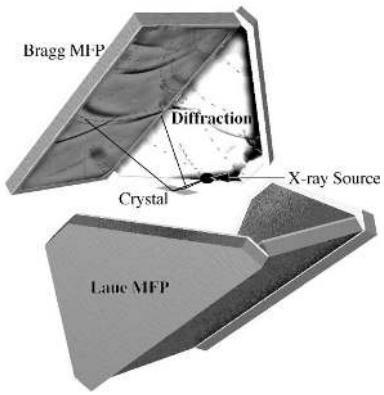

FIG. 13: Schematic diagram of the experiment setup. A point source of x-rays is placed close to a single crystal. The diffracted signal from the crystal is recorded by wide angle film packs which can cover nearly 2π of solid angle. The film packs are placed to record reflected diffraction (Bragg geometry) and transmitted diffraction (Laue geometry).

VI. EXPERIMENTAL RESULTS AND ANALYSIS

As discussed briefly in the previous section the diverging quasi-monochromatic point source of X-rays covers a range of angles across the crystal surface, $\approx 20^o$ to $\approx 70^o$ cylindrically symmetric about the X-ray source. X-rays are diffracted from the crystal, and recorded on the MFP wherever the Bragg condition is met:

$$\lambda_o = 2d_{hk(i)l} \sin\theta, \tag{2}$$

where λ is the x-ray wavelength, $d_{hk(i)l}$ is the spacing of the (hk(i)l) planes, and θ is the angle with respect to the plane from which the x-rays are diffracted. Due to the divergence of the source, the large angle the crystal subtends to this source, and the large solid angle recorded by the MFPs, information about the spacing of many planes is recorded simultaneously. Compression of the crystal results in changes in plane spacing $d_{hk(i)l}$ and normal directions, which in turn change the Bragg angle and shift the recorded diffraction lines on the film. On nanosecond time-scales, the shock propagates through the parylene ablator and into the first few mircons of iron, which is comparable with the absorption depth for the iron K-shell X-rays within the iron crystal. By varying the timing of the X-ray pulse with respect to the shock generation pulse, it is possible to record X-rays diffracted from un-shocked material (ahead of the shock), shock-compressed BCC material, and, as will be shown, (for high enough shock pressures) shock-compressed HCP material simultaneously.

Typical raw-data recorded images on the MFPs are shown in Fig. 14. Figure 14(a) shows a diffraction signal from both the shocked and unshocked BCC lattice on a single piece of film at a pressure of 5.4 GPa, below that required for the $\alpha-\epsilon$ transition. The regions where diffraction occurs on the crystal surface are conic sections and the diffracted X-rays form arcs on the film, where the location on the film and curvature of the arc give information about the plane orientation and lattice spacing [36]. The Miller indices of the diffracting planes are shown for the raw data both for the unshocked material ('static') and shocked crystal ('compressed'). Figure 14(b) is a sample of raw data at a pressure of 26 GPa, above that required for the $\alpha - \epsilon$ transition. Note that, for example, the arc corresponding to diffraction from $(002)_{\mathrm{BCC}}$ is now split into three components – the first corresponding to diffraction from unshocked BCC, the second to shock-compressed BCC, and the third to a further region of compression which we have attributed to the associated diffraction from the HCP phase, as discussed below.

Analysis of the diffraction images is performed by comparing the experimental data to predicted patterns calculated by ray tracing. Within the raytracing routine the location and wavelength of the x-ray source, location and orientation of the crystal and crystal planes, and the location of the film are fixed for the specific crystal type. The location on the crystal surface where the Bragg condition is met is calculated for all possible diffracting planes, $2d_{hk(i)l} \gg \lambda$. Then, knowing the location on the crystal from which the diffraction occurs and the relevant Bragg angle, the location of the x-rays incident on the film is calculated. Compression and/or rotation of any of the three lattice types along or around any lattice vector is also modeled.As the structure, lattice spacing of the unshocked crystal is known and the orientation with respect to the physical surface of the crystal (to within $\pm 1^{\circ}$), diffraction from an unshocked sample can be used to fit the relative location and orientation of the source, crystal, and detector.

Once the source, detector, and crystal positions and orientations have been identified, the compression and/or rotation of the unit cell of the crystal is modified in the ray tracing routine to determine the lattice parameters and orientation that best fit the diffraction lines due to the shock compressed crystal. For example, for the data shown in Figure 14(a) at 5.4 GPa, we find that all of the diffraction lines can be well-fitted assuming the compression along the shock propagation direction (i.e $[001]_{\mathrm{BCC}}$) direction is 4.1%±0.3%. This compression is most easily inferred from the shift of the $(002)_{\mathrm{BCC}}$ plane. This compression along $[001]_{\mathrm{BCC}}$ also immediately gives an excellent fit to the $(112)_{\mathrm{BCC}}$ line of the shock compressed crystal. As the reciprocal lattice vector associated with this plane has a component perpendicular to the shock propagation direction, this implies purely elastic compression of the lattice, as observed in the NEMD calculations.

Taking sample data at 12 GPa the best fit uni-axial compression from the $(002)_{\mathrm{BCC}}$ lines is 5.2%±0.2%. Assuming only uni-axial compression the $(112)_{\mathrm{BCC}}$ plane suggests 5.0% ±0.2% and $(1\bar{1}2)_{\mathrm{BCC}}$ plane suggests 5.7% ±0.4%. Fixing the compression along the shock direction at 5.2% from the (002) plane, the lateral deformation can be estimated as a 0.3%±0.5% expansion and 0.4% ±0.5% compression by the $(112)_{\mathrm{BCC}}$ and $(1\bar{1}2)_{\mathrm{BCC}}$ planes respectively. A similar analysis of a 13 GPa shot shows compression in the shock direction of 5.8% ±0.3% with the lateral compression estimate of 0.3% ±0.6% expansion and 0.1% ±0.6% compression again for the $(112)_{\mathrm{BCC}}$ and $(1\bar{1}2)_{\mathrm{BCC}}$ planes respectively. Within the uncertainty of the measurement, the lack of plasticity before the phase transition agrees well with the MD

simulations, even though the experimental time scale is orders of magnitude longer than the simulation. Note that this elastic compression of the BCC lattice was observed in all the data we obtained, including that where the HCP phase was also observed. Plastic behavior was observed only in some of the 10 μm thin foil samples probed by Laue diffraction, these will be addresses later.

This lack of plasticity of the crystal contrasts with the wave profiles of shocked Iron observed on microsecond time-scales [7, 39]. In these longer time-scale experiments, a three-wave structure is often observed – the first being associated with the HEL, the second with an elastic-plastic transition, and the final wave associated with the phase transition itself. Our experiments are, on the one hand, recording data on a time-scale two-orders of magnitude longer than the MD simulations, but on the other hand perhaps three orders of magnitude faster than that normally associated with shock-wave experiments. The exact time-scale for plastic behavior in shock-compressed iron thus remains an interesting issue.

At the lowest laser intensities, and thus the lowest applied pressures, only unshocked and elastically compressed BCC diffraction lines were observed. As the laser intensity, and thus shock pressure, is increased, the diffraction lines corresponding to the shocked BCC indicate higher compressions. The pressure applied by the laser ablation of the plastic overcoat was not directly measured in these experiments. However, knowing from the diffraction data that the compression at the lowest pressures is purely elastic, we can infer the pressure for each experiment based on the 3$^{\rm rd}$ order elasticity [40]. The pressure is then scaled to higher laser intensities and different wavelengths based on scaling relations at these intensities calculated by LASNEX

At the highest shock pressures a third line is evident in the diffraction associated with the original (002) plane, as can be seen in Fig. 14(b). This third feature is observed only above a threshold pressure of approximately 13 GPa. The feature corresponds to a compression of the $(002)_{\rm BCC}$ planes by bewteen 15 and 18%, depending upon the applied pressure. The diffraction in this region is broader and more diffuse than the diffraction associated with the unshocked lattice, and the compressed BCC lattice. We discuss the width of this line further in section VII. The appearance of this 3$^{\rm rd}$ arc is correlated to additional features such as the appearance of an arc consistent with the period doubling of the $(112)_{\rm BCC}$ plane in the Bragg geometry. This is labelled by its HCP indices as $(1\bar{2}10)_{\rm HCP}$ in Fig. 14 b). This type of period doubling is consistent with the shifting of alternate $(110)_{\rm BCC}$ planes described in

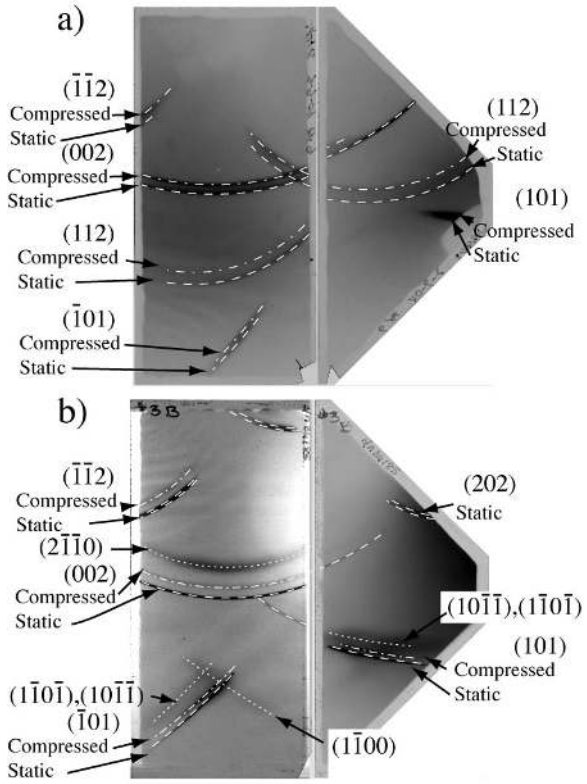

FIG. 14: Two complete data sets with the diffraction planes labeled with Miller indices labelled in the BCC and HCP case. NOTE: degenerate planes are identified with labels for both possible HCP orientations. a) at 5.4 GPa shows diffraction from static (dashed line), and compressed (dashed-dotted) iron. b) at 28 GPa the static (dashed line), compressed (dashed-dotted line) and mean phase (dotted line) are labeled.

earlier section II.

Due to the geometrical constraints of the experimental setup there is only one feature consistent with the period doubling associated with the HCP phase in Bragg reflection geometry. The transmitted Laue diffraction using thin crystals provides further information about the structure of the shock-compressed crystals. Figure 15 shows the diffraction in the Laue transmission geometry when the crystal is shocked below the transition pressure. The overlaid lines and labels indicate the specific lattice plane with the corresponding Miller indices. In contrast, Fig 16 shows the data for a crystal shocked above the phase transition. Note that two new diffraction lines appear correspond to the $(0\bar{1}11)_{\mathrm{HCP}}$ and $(01\bar{1}1)_{\mathrm{HCP}}$ reflections of the HCP phase, each consistent with a different orientation of c-axis.The appearance of both of these reflections indicates that the single crystal BCC lattice has transformed to

an HCP structure with small regions where the c-axis is oriented along the original $[110]_{\mathrm{BCC}}$ direction, and other parts where is it oriented along the original $[1\bar{1}0]_{\mathrm{BCC}}$ direction, as described in section II. The nearly equal intensity of the lines suggests that the amount of crystal in each orientation is approximately equal. The lines in Fig 16 have been labeled to distinguish between the two possible orientations of the HCP lattice.

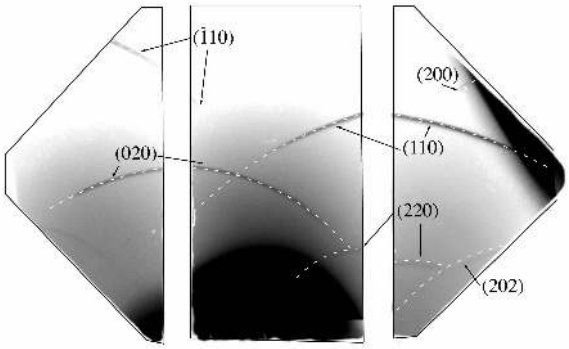

FIG. 15: Data image showing the Laue diffraction recorded through a 10μm single crystal iron sample shocked at a pressure of 3.6 GPa. There is no shift in the diffraction planes perpendicular to the shock direction.

The Laue diffraction also provides information about the atomic motion perpendicular to the shock. The location of the lines are consistent with no lateral compression of the atoms upon the $\alpha - \epsilon$ transition. The width of the lines and non-uniformity of the thin samples makes it difficult to extract quantitative information about the lateral motion of the atoms. This suggests that the HCP lattice does not form a perfect hexagon in the $(110)_{\mathrm{BCC}}$ plane. Instead, like the MD simulations the shift of atoms which cause the period doubling of the BCC lattice to make HCP occurs yielding an imperfect HCP lattice. This is contrary to case of hydrostatic compression Wang and Ingalls observed, suggesting a single value of 1.6 is reached for the c/a ratio over a small pressure range.

The volume compression of the lattice is plotted as a function of shock pressure in Fig. 17. As both the shock-compressed BCC and HCP material are observed uniaxially compressed, the volume is simply determined as the lattice spacing parallel to the shock direction. For the uniaxial deformation up to 6%, this is from the spacing of the $(002)_{\mathrm{BCC}}$ planes of the initial bcc lattice with an uncertainty of approximately 0.003. For the 15%–18% compressions, this was determined as the spacing of the $(2\bar{1}\bar{1}0)_{\mathrm{HCP}}$ planes with an uncertainty of approximately

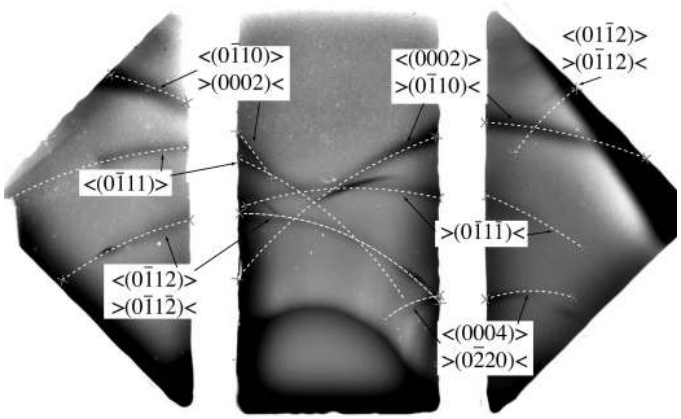

FIG. 16: Data image showing the Laue diffraction recorded through a 10μm single crystal iron sample shocked at 13.8 GPa, above the transition threshold. The diffraction shows considerable broadening of the lines similar to the HCP lines identified in the Bragg geometry, plus the addition of two lines consistent with an HCP structure. The two different orientations are denoted by beginning the fitted line with $\langle -\rangle$ arrows for one orientation $\rangle - \langle$ for the other and $\times - \times$ for lines which are consistent with both. The labels are bracketed by the same symbol as the line to denote the label for a given orientation.

0.01–0.02.

In this figure we have made a distinction between the compressed BCC when it appears on its own (solid triangles), and when it appears simulatneously with the HCP feature (open triangles and open squares respectively). If we interpret the observation of diffraction from both compressed BCC and the HCP as diffraction from a two-wave structure, similar to the NEMD simulations, then the pressure in the compressed BCC is not the peak applied pressure shown. Instead, the pressure in this first wave should correspond to the transition pressure. The uniaxial compression of the BCC lattice shows a maximum of 6-7%, consistent with a transition pressure of 130 GPa [7]

A. The Mechanism

Our analysis of the NEMD simulation results showed that there is no rotation of the HCP lattice with respect to the original BCC lattice – thus supporting Mechanism I′. We show in this section that an analysis of the experimental data leads to the same conclusion.

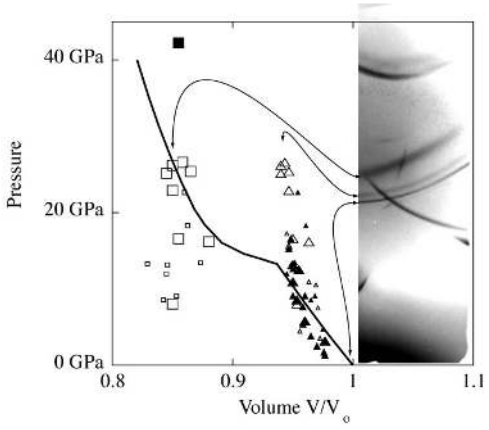

FIG. 17: Plot of the peak pressure versus volumetric compression calculated from the shift in the diffraction lines. The solid triangle represent measurements where only the compressed BCC line was present, the open triangle (BCC) and open square (HCP) represent measurements made when both BCC and HCP where observed simultaneously. The solid square shows the case where only the HCP feature was observed. The symbols are shown in three different sizes for each shape, large denotes measurements made with a 351nm drive, medium 532nm drive, and small 1063nm drive. The room temperature shock Hugoniot is overlaid as a solid line.

As described earlier a change in the lattice plane spacing will cause the corresponding arc on the film to change position and curvature, as the curvature is determined by Bragg angle which changes with plane spacing. A rotation or change in orientation of the plane will change the orientation of the arc with respect to that of the original BCC lattice. We will know look at the possible degree of rotation allowed with in the experimental data and how that corresponds to the transition mechanisms described in section II.

In section II two differentiable mechanisms for the phase transition where described. One in which the HCP end state has the $(2\bar{1}\bar{1}0)_{\mathrm{HCP}}$ parallel to the initial $(002)_{\mathrm{BCC}}$, with different spacing, the other two where $(2\bar{1}\bar{1}0)_{\mathrm{HCP}}$ has upto an angle of 5°with respect to the initial orientation of $(002)_{\mathrm{BCC}}$. Figure 18 shows the diffraction pattern from a 23 GPa shocked sample which has undergone the phase transition. Due to the degeneracy of the shift along the $\{110\}_{\mathrm{BCC}}$ family of planes there are 4 variants of the rotation of the $(2\bar{1}\bar{1}0)_{\mathrm{HCP}}$ plane. The Laue diffraction has shown that the transformed HCP crystal is polycrystalline suggesting that if Mechanism II′ or IIa′ are responsible for the transition that all four rotations would

have occurred. Fitting the HCP lines by different compressions for the 4 degenerate rotations is unphysical. We therefore compare the data with an overlay of the 4 rotations assuming a single compression. The relative shift of the 4 degenerate lines is shown in Fig. 18 assuming a 5°rotation of the HCP lattice upon phase change. This significantly over predicts the the width of the diffraction lines.

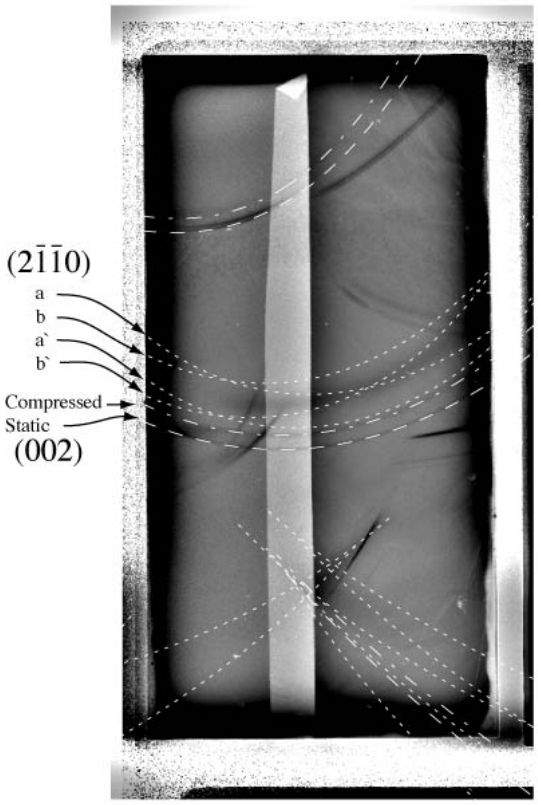

FIG. 18: Diffraction data image of a 27 GPa shock compressed iron sample with overlaid lines accounting for the 5°rotation prediction assuming Mechanism II′ or IIa′. The a and b denote the different HCP orientations, the prime denotes the -5°rotation for each of the orientations.

As we see from section III B, even if the BCC crystal is pre-compressed elastically by 6%, a rotation of 3.5°is still required by Mechanism II′ or IIa′ to create a hexagonal structure. Figure 19 shows line outs from the data with overlays calculated assuming a range of lattice rotations. The arrows denote the position of the diffraction lines assuming no broadening. The simulated line outs are broadened and scalled to obtain a best fit with the data. It is apparent that a rotation larger then 2°would not be consistent with data. This rotation is

too small for Mechanism II′ or IIa′ even taking into account a unperfect hexagonal structure upon transformation. Thus we conclude that the experimental data is consistent with transformation Mechanism I′.

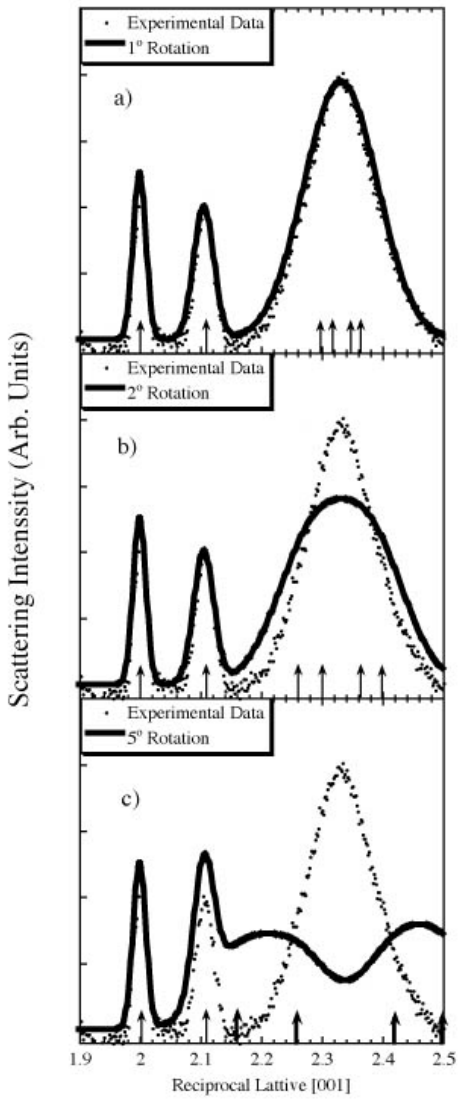

FIG. 19: Lineouts showing the compression of the $(002)_{\mathrm{BCC}}$ lattice plane fitted by various degrees of rotation between the HCP and BCC lattices. At 2°, the width of the fitted line exceeds that of the experimental lineout.

B. Eliminating the possibility of an FCC structure

We have in the preceding sections deduced that the new diffraction features observed upon shock compression indicate the HCP-like close-packed phase. However, FCC is also a close-packed structure that can exist over a wide region of temperatures, and indicated from the phase diagram for iron shown in Fig. 1.Whilst the hugoniot (for a crystal originally at room temperature), also shown in Fig. 1 does not pass through the γ phase, we consider the possibility that such a phase might be formed. Recent MD simulations indicate that a considerable fraction of shock-compressed single-crystal iron can transform to the γ phase if the crystal is shocked along the [110] or [111] directions [41]. Thus, before conclusively stating that the data confirms an HCP-like structure, it is important to eliminate the possibility that the data supports an FCC phase.

An FCC lattice can be generated by compressing along the $[001]_{\mathrm{BCC}}$ axis to obtain a perfect hexagon in the $(110)_{\mathrm{BCC}}$ plane, then instead of shuffling alternate $(110)_{\mathrm{BCC}}$ planes we shuffle pairs of $(110)_{\mathrm{BCC}}$ planes in alternate directions to obtain the ABCABC...stacking of FCC. This will leave us with a FCC structure with a cell size of $a_{\mathrm{FCC}} = \frac{2}{\sqrt{3}}a_o$, oriented such that the hexagon is in the $(1\bar{1}1)_{\mathrm{FCC}}$ plane, as shown in Fig. VI B. The directions and planes in FCC that correspond to those in BCC are then $[110]_{\mathrm{FCC}} \| [001]_{\mathrm{BCC}}$, $(\bar{2}\bar{1}\bar{1})_{\mathrm{FCC}} \| (\bar{1}12)_{\mathrm{BCC}}$, and $(220)_{\mathrm{FCC}}$ will match $(002)_{\mathrm{BCC}}$. Note: Fig. fig:FCCPhaseChange also shows that the stacking of the FCC lattice is such that the $(112)_{\mathrm{BCC}}$ plane becomes forbidden, as does the $(\frac{1}{2}\frac{1}{2}1)_{\mathrm{BCC}}$ plane which corresponds to the $(1\bar{1}00)_{\mathrm{HCP}}$ plane seen in Fig. 14.

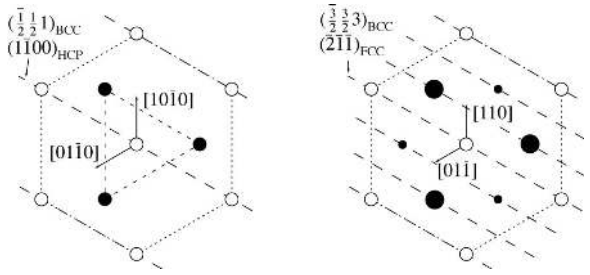

FIG. 20: A comparison of the possible HCP and FCC end states. This shows the $(0002)_{\mathrm{HCP}}$ or $(1\bar{1}1)_{\mathrm{FCC}}$ plane. The atoms of different color and size denote different $(0002)_{\mathrm{HCP}}$ or $(1\bar{1}1)_{\mathrm{FCC}}$ planes. Note the HCP allows diffraction from the $(\bar{\frac{1}{2}}\frac{1}{2}1)_{\mathrm{BCC}}$ plane where the FCC allows diffraction from the $(\bar{\frac{3}{2}}\frac{3}{2}3)_{\mathrm{BCC}}$.

Figure 21(a) shows the fitting of one diffraction image assuming an HCP lattice with only uni-axial compression, and no lateral movement other then the shuffle of the atoms. For all cases that show the period doubling this hypothesis fits the data very well.

The same data is fit assuming an FCC lattice with its (101) plane parallel to the initial (002) plane. Figure 21 (b) shows that for this shot in the Bragg geometry that the best FCC fit allowed by compression does not generate diffraction lines seen within the data that can be matched by an HCP lattice, i.e. the ones consistent with $(1\bar{1}00)_{\mathrm{HCP}}$ and $(10\bar{1}0)_{\mathrm{HCP}}$ planes. The reason why the FCC structure will not generate the new lines to match the experiment is that both FCC and BCC have one atom per unit cell, meaning that the density in reciprocal lattice space of the diffraction planes is the same (with only a slight change due to compression). HCP as two atoms per unit cell making the density of diffraction planes in reciprocal space double that of the BCC or FCC. So while a transition from the BCC to FCC lattice will move the diffraction planes to new locations, it will not increase the number of diffraction planes recorded. To accommodate the appearance of new diffraction planes iron single crystal shocked along the $[001]_{\mathrm{BCC}}$ direction would have to expand in volume by 21% in the transition from BCC to FCC to match the diffraction lines.

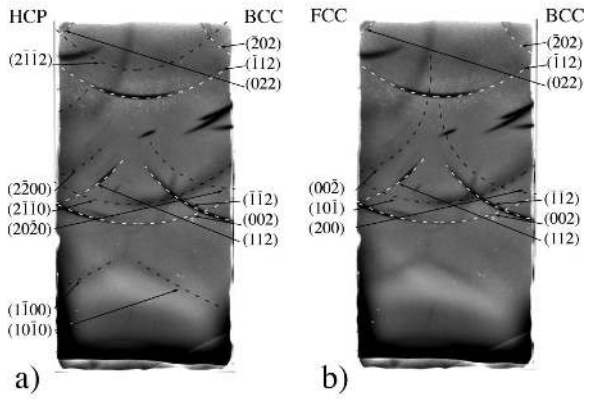

FIG. 21: Diffraction from a shock compressed iron sample at 19 GPa fitted with a) an HCP structure with the relations put forward by Burgers. b) restricting the FCC to have a net compression the lines which appear upon compression can not be fitted.

The experiment and the NEMD simulations show consistent features in their analysis. Both show the $\alpha - \epsilon$ phase change above a threshold pressure, a polycrystalline HCP final phase and a transformation which is consistent with Mechanism I′. We will demonstrate

the similarities in the widths of the diffraction peaks and exploit these similarities to make some inferences of the microstructure of the crystal in the experiment in the next section.

VII. GRAIN SIZE

Up until now we have analyzed the NEMD simulations and experimental data separately, sections IV and VI respectfully. In this section we will show the similarities between the NEMD simulations and the experiment are very good and will use the NEMD simulations, where we know the location of every atom, to get a deeper understanding of the experimental data, particularly where the broadening of the HCP lines come from and the timescale to transform from a compressed BCC lattice to an HCP lattice.

A 3D Fourier transform was calculated on the atomic positions for the NEMD simulation described earlier for a small volume surrounding the $(2\bar{1}\bar{1}0)_{\mathrm{HCP}}$ spot (including the compressed $(002)_{\mathrm{BCC}}$ peak but not the static peak) .This reciprocal density space was integrated over the $[010]_{\mathrm{BCC}}$ and $[100]_{\mathrm{BCC}}$ directions to give the projection along the $[001]_{\mathrm{BCC}}$ shock direction. Figure 22 shows the 3D Fourier transform (inset), a two dimensional slice through the (002) peaks, and the integrated projection on the $[001]_{\mathrm{BCC}}$-axis of the MD simulation. This is compared with a lineout through the experimental data. There is excellent agreement between the MD simulation and experiment. Both show sharp, well defined BCC static and compressed peaks and a broad $(2\bar{1}\bar{1}0)_{\mathrm{HCP}}$ peak. Note that, the broadening of the simulated peak is due to the finite number of atoms in the BCC state along the compressed direction, and the broadening in the experiment is due to the finite width of the iron K-shell doublet used to probe the iron. The FWHM of the simulated $(2\bar{1}\bar{1}0)_{\mathrm{HCP}}$ peak is 0.1 reciprocal lattice units while the experiment is 0.2, giving good agreement between simulation and experiment. The similarities between the experimental data and the NEMD simulations give us confidence that we can use a microscopic analysis of the NEMD simulations to better understand the broadening of the $(2\bar{1}\bar{1}0)_{\mathrm{HCP}}$ diffraction line in the experiment. This peak is taken as representative of the data because over a wide range of laser parameters and drive intensities there is little variation of the HCP peak width.

While discussing the mechanism of the phase change in the NEMD in section IV we showed that the relative angle between adjacent atoms in the shock direction in the HCP crystallites do not vary more than is expected from thermal vibrations , Fig. 12. Figure

12 showed the angular orientation for the three cases which had a transition and a case of a compressed crystal at a temperature of 500K. Figure 23, shows the separation of nearest neighbor atoms for the transitioned region in the three NEMD simulations as well as the nearest neighbor distribution for a compressed HCP sample at 500K. The location of the nearest neighbor atoms is consistent with thermal broadening. If there was a range of compressions the nearest neighbor spacing would be broader. If the angle varied between grains or the compression between grains or within a grain of HCP these would cause broadening of the HCP diffraction peak, but thermal vibrations will cause broadening in the local angle distribution and nearest neighbor distance but will not cause broadening in the diffraction peak. Thermal vibrations only change the relative intensity between peaks through the DeBye-Walla factor. These calculations were integrated over a large volume of the simulation containing many grains, so the broadening does not appear to come from rotation or variation in compression between different grains. The NEMD simulation suggests that in the transitioned HCP lattice the compression and orientation can not explain the broadening observed of the HCP diffraction peak, we suggest that the broadening is due to the grain size of the HCP grains. As discussed in section IV the reciprocal lattice space of the NEMD simulations showed features consistent with both possible orientations of the c-axis. Regions of different c-axis orientation would cause the HCP to have a polycrystalline structure.

Finite crystallite size will lead to broadening of the diffraction peaks shown in Fig. 22. Fitting the simulated x-ray diffraction from the MD output with a analytically calculated diffraction spectrum broadened by finite grain size suggests a 4 nm grain size in the NEMD simulations[42], Fig. 24. This is consistent with counting grain boundaries through the simulated sample.

Like the NEMD simulation the experiment shows diffraction which is consistent with a polycrystalline HCP end state. The nearly equal intensities of the recorded diffraction lines suggests that both states are present in equal amounts. Again, like the NEMD we have a single crystal BCC sample becoming a poly-crystalline HCP upon the phase transition. Based on the analysis of the NEMD we assume that the broadening is only due to grain size effects. There could is the possibility of variations in pressure, but generally these would be do to hot spots in the beam at a particular location, causing variations in pressure laterally across the sample, only significant temporal variations would cause the pressure to vary as a function of depth. A variation in pressure as a function of time is not observed because of

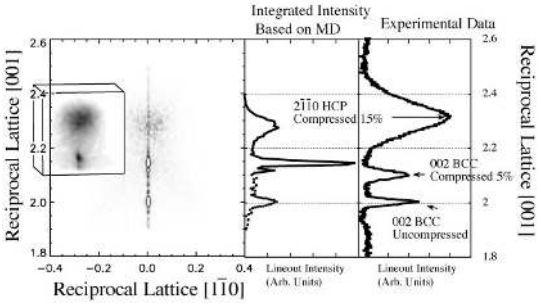

FIG. 22: Comparing the width of the peak from the post-processed NEMD simulations and the experimental data. The far left is a 2D close up of the $(002)_{\mathrm{BCC}}$ / $(2\bar{1}\bar{1}0)_{\mathrm{HCP}}$ spot with a 3D image inset. This is compared with a lineout from the experimental data converted to reciprocal lattice units.

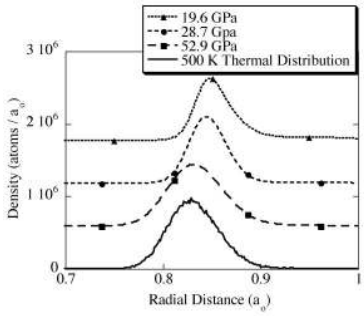

FIG. 23: The radial distribution function around each atom close to one unit cell away. Three shocked cases and a perfect HCP crystal at 500K are plotted, with a base line offset for clarity. The broadening of the shocked samples is consistent with thermal broadening.

the sharp compressed BCC peaks, even in the cases where the applied pressure was below the transition pressure. The amount of broadening due to a variation in pressure is quite small. Also a variation in pressure would not explain the broadening of the lines recorded in the Laue geometry because these are orthogonal to the shock direction. The reproducibility of the peak width over a range of laser intensities and experimental sights suggests it is a physical phenomena fundamental to the transition and not a temporal variation in the experimental drive. Fitting the experimental diffraction data with the same analytical model to predict the broadening due to grain size effects suggests a grain size of only 2 nm, shown in

Fig. 24. Using the diffraction from the perfect BCC crystal to get an estimate of instrument broadening due to the wavelength range of the x-ray source, the smallest possible grain size will range from 2-2.5 nm assuming that the only source of broadening due to the grain size. The presence of other sources of broadening would mean the grain size is larger.

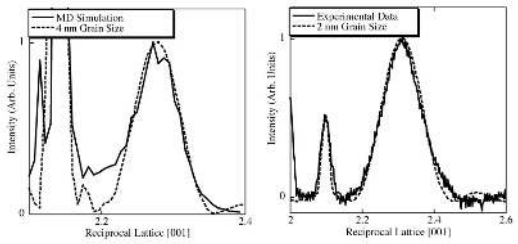

FIG. 24: a) A plot of a lineout along the reciprocal lattice $[001]_{\mathrm{BCC}}$ of the post-processed NEMD simulations and a fitted with an analytic calculation of the diffraction spectrum of a crystal with 4 nm grain size. The difference in the region between the two peaks is attributed to the transition region between the compressed BCC state and the HCP state. b) Shows a similar plot for experimental data fitted with an analytic diffraction spectrum from a crystal with 2 nm grain size.

VIII. TIMESCALE

The timescale that the lattice transforms from compressed BCC to the HCP in NEMD simulations can be estimated based on the shock speed and the volume of the sample between the compressed BCC region and HCP region. Looking at a density profile of a 19.6 GPa shock we estimate the transition region is smaller then 25 unit cells (shown as the shaded region in Fig. 25). Using the shock velocity of 5.4 km/sec [25] the transition time from compressed BCC to HCP is on the order of 1.5 ps, faster for the higher shock pressures. This is a measurement of the bulk volume collapse in of the $\alpha - \epsilon$ transition in the NEMD simulation, as a second wave behind the elastic compression.

Looking at the NEMD simulated x-ray diffraction signal in Fig. 24 there are considerable signal levels between the HCP and BCC peaks which can not be matched by the analytic fit for the finite grain size broadening. Taking the difference between the analytic scattering for a crystal with a finite grain size, but otherwise perfect crystal, and the post-processed MD signal, 6% of the total scattering is not consistent with the analytic scattering with

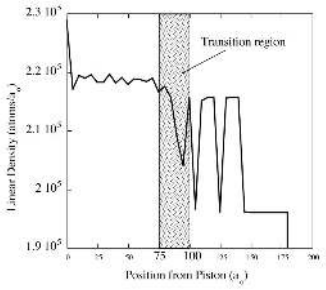

FIG. 25: A plot of the density as a function of location in the crystal. The highlighted region is the region where the matterial under goes a volume collapse and becomes HCP.

finite grain size effects. A large component of this will come from the region in the NEMD simulation where the atoms are reorganizing to an HCP lattice from the BCC lattice, i.e. as the $(002)_{\mathrm{BCC}}$ plane is collapsing to the $(2\bar{1}\bar{1}0)_{\mathrm{HCP}}$). Given that the transition occurs over approximately 13% of the total number of atoms in the 19.6 GPa simulation we can use the amount signal levels from the experiment which deviates from a finite grain size spectrum to estimate the size of the transition region.

To first order the x-ray diffraction measurements in the experiment place an upper bound on the transition time of 2 ns, because the x-ray pulse is on for 2 ns and can record both static, compressed and phase changed material in a single pulse. Fitting several shots over a range of pressures with a finite grain size yields the scattering of the transition region to account for at most 3±1% of the total scattering. This suggests that upto 6% of all of the atoms probed are in the transition region. In the real experiment the x-rays diffracting from the $(002)_{\mathrm{BCC}}$ plane at 40.4°will penetrate a $1/e$ depth of 7 μm into the sample. Since there are other possible causes for signal to occur between the compressed BCC peak and the HCP peak it sets an upper bound on the bulk transition time of 80 psec, where locally the atoms may shift faster.

IX. DISCUSSION

In-situ nano-second X-ray diffraction was used to study the iron $\alpha-\epsilon$ phase transition under shock compression. in experiments and NEMD simulations. Post-processing the NEMD simulations with a Fourier transform allows a direct comparison of the NEMD simulations

with the experimental data as this effectively creates a simulated X-ray diffraction diagnostic. This type of post-processing also gives the long range correlation between the atoms, to study the poly-crystalline nature of the ϵ-phase. The NEMD simulations and experiment both show the atoms undergoing an initial uni-axial compression before the $\alpha - \epsilon$ transition which requiring a shift of alternate (110) planes. The simulation and experiment are both consistent with the transition occur via Mechanism I′, where only compression along the $[001]_{\mathrm{BCC}}$ direction is responsible for generating a pseudo-hexagon in the $(110)_{\mathrm{BCC}}$ plane, as Mechanism II′ causes a net angle to occur between the orientation of the initial BCC lattice and the transitioned HCP lattice which was not consistent with the NEMD or experimental data. Given the similarities between the diffraction in the experiment and the diffraction from the simulation we used a microscopic analysis of the NEMD to explain features observed in the experimental data. From this analysis we conclude that the final HCP state is polycrystalline with a grain size of 2-2.5 nm (4 nm in the MD).The lack of signal between the compressed BCC and HCP suggest a transition time faster than 80 ps (1.5 ps in the MD).

One interesting result that warrants further discussion is the lack of plasticity in the compressed BCC iron before it undergoes the phase change. Gas gun shocked experimental measurements using VISAR have shown the characteristic three wave structure associated with elastic and plastic compression and a phase change. Even the original Bancroft work resolved the three wave structure. There can be many possible reasons for this difference. The diffraction probes $\approx 7\mu m$ into the sample, which is a small region compared to the samples studied in gas gun work. It may be that the transition from elastic compression to plastic requires some time scale which on the timescale of the diffraction experiment (2 ns) is too long to diagnose. The diffraction suggests that at the driven surface there is no plastic wave, it is possible that it requires a longer distance in the sample to get a large enough separation between the plastic and phase transition wave to record each seperately. Other drive techniques may offer a method to maintain the pressure on the sample for longer time-scales and study the elastic plastic transition in iron [43, 44]. The plastic effects may depend on the sample itself. Most previous work on iron samples were done with poly-crystalline samples, while the diffraction experiments require a single crystals. The different crystal type may react differently to the shock loading. In these experiments two types of single crystals where used, thick samples which where grown from a melt process, and thin

samples where where vapor deposited on a single crystal substrate. While the thin samples provide excellent qualitative data, because they allow Laue diffraction measurements to be made, they general generate diffraction lines which are broken and difficult to fit with a single crystal model (with upto a 3^o rotation of the crystal to fit different lines on the same piece of film) as oppose to the thick crystals which generate patterns that can be match with a single crystal. The thin crystals being only 10 μm thick are more susceptible to lattice deformation from the handling required to assemble targets. Generally this may cause bends in the crystals, that make regions of the sample diffract to different locations then expected on the film and would lead to dislocation generation. Figure 26, is a 11 GPa shot where the features characteristic of the phase transition where not observed, but the Laue pattern shows some compression latteral to the shock direction. Measuring the shift of a single line in the Laue film suggests a 2.4% $\pm$0.3% compression normal to the shock direction which agrees well with the information in the Bragg geometry where the compression along the shock direction measured by the change in spacing of the $(002)_{\mathrm{BCC}}$ is 3.8% $\pm$0.2% and the lateral compression measured by $(\bar{1}\bar{1}2)_{\mathrm{BCC}}$ is 2.3% $\pm$0.6% and 2.8% $\pm$0.6% by $(112)_{\mathrm{BCC}}$, for a total volume compression of 9% $\pm$1%. So in this case there is no evidence of phase change but plastic deformation. Understanding how the initial crystal state affects the final state and the possible intermediate states is a continued area of research.

Not only varying defect density in the sample but the crystal orientation will provide more information about the iron $\alpha - \epsilon$ transition. This article looks at the compression of single crystal iron along a single crystallographic axis, which may help drive the Mechanism I′ as it provides a method of preferentially compressing the $[001]_{\mathrm{BCC}}$-axis generating two possible directions for the c-axis in the HCP . Recent MD simulations suggest that by altering the shock direction that the material response at the atomic level changes [41], i.e. the grain structure and lattice characteristics change. By shocking along the $[110]_{\mathrm{BCC}}$ direction in the crystal the transition appears to favor the γ (FCC) phase over the HCP, similar along the $[111]_{\mathrm{BCC}}$. This presents an interesting question about the resulting end phase for a given transition and what this would mean in a polycrystalline sample where the grains are oriented randomly with respect to the shocking direction. Continuing effort is being placed on simulation and experiment to understand the effect of shocking along different crystal axis.

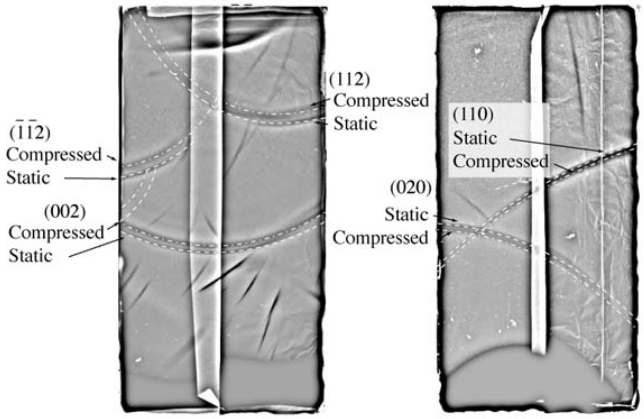

FIG. 26: Data images of Laue and Bragg diffraction taken simultaneously from the same iron crystal sample which was 10 μm thick, showing that there is some lateral compression of the lattice for some thin samples.

X. ACKNOWLEDGEMENTS

The authors would like to thank the staff at the Vulcan Laser Facility at the Rutherford Appleton Laboratory, the staff at Janus laser at Lawrence Livermore National Laboratory and the staff and LLE University of Rochester. This work was conducted under the auspices of the U.S. DOE by the UC LLNL and LANL under Contract No. W-7405-Eng-48. Experiments were conducted at the University of Rochester Laboratory for Laser Energetics under the NLUF grants program. Additional support was provided by the DOE under Grants No. DEFG0398DP00212 and No. DEFG0300SF2202, by the U.K. EPSRC under Grant No. GR/R25699/01, by the Advanced Simulation and Computing Materials and Physics Modeling program and LDRD-DR 20020053 at LANL, and by the LDRD program Project No. 04-ERD071 at LLNL. The authors would also acknowledge useful discussions with Jon Eggert, Gilbert Collins, and Bruce Remington.

---

[1] P. W. Bridgman. *Collected experimental papers.* Harvard University Press, Cambridge,, 1964. [by] P.W. Bridgman. illus. 25 cm. Some papers in German. "In most cases the original reprints

have been reproduced photographically, although in a few instances it proved necessary to reset a paper in type.".

[2] Michael I. Bergman. Measurements of electric anisotropy due to solidification texturing and the implications for the earth's inner core. *Nature*, 389(6646):60, 1997.

[3] D. H. Kalantar, J. F. Belak, G. W. Collins, J. D. Colvin, H. M. Davies, J. H. Eggert, T. C. Germann, J. Hawreliak, B. L. Holian, K. Kadau, P. S. Lomdahl, H. E. Lorenzana, M. A. Meyers, K. Rosolankova, M. S. Schneider, J. Sheppard, J. S. Stolken, and J. S. Wark. Direct observation of the alpha-epsilon transition in shock-compressed iron via nanosecond x-ray diffraction. *Phys. Rev. Lett.*, 95(7):075502, 2005.

[4] B. Yaakobi, T. R. Boehly, D. D. Meyerhofer, T. J. B. Collins, B. A. Remington, P. G. Allen, S. M. Pollaine, H. E. Lorenzana, and J. H. Eggert. Exafs measurement of iron bcc-to-hcp phase transformation in nanosecond-laser shocks. *Phys. Rev. Lett.*, 95(7):075501, 2005.

[5] J.M. Walsh. *Bulletin of the American Physical Society*, 29:28, 1954.

[6] P. W. Bridgman. The measurement of hydrostatic pressure to 30,000 kg/cm2. *Proceedings of the American Academic Arts and Sciences*, 74:11–20, 1940.

[7] D. Bancroft, E. L. Peterson, and S. Minshall. Polymorphism of iron at high pressure. *Journal of Applied Physics*, 27(3):291–298, 1956.

[8] S. Minshall. Investigation of a polymorphic transition in iron at 130 k.b. volume 98, page 271, 1955.

[9] P. W. Bridgman. High pressure polymorphism of iron. *Journal of Applied Physics*, 27(6):659, 1956.

[10] S. K. Saxena and L. S. Dubrovinsky. Iron phases at high pressures and temperatures; phase transition and melting. *American Mineralogist*, 85(2):372–375, 2000.

[11] C. S. Yoo, N. C. Holmes, M. Ross, D. J. Webb, and C. Pike. Shock temperatures and melting of iron at earth core conditions. *Phys. Rev. Lett.*, 70(25):3931–3934, 1993.

[12] J. C. Boettger and D. C. Wallace. Metastability and dynamics of the shock-induced phase transition in iron. *Physical Review B*, 55(5):2840–2849, 1997.

[13] J.C. Jamieson and A. W. Lawson. X-ray diffraction studies in the 100 kilobar pressure range. *Journal of Applied Physics*, 33(3):776–780, 1962.

[14] J. F. Lin, O. Degtyareva, C. T. Prewitt, P. Dera, N. Sata, E. Gregoryanz, H. K. Mao, and R. J. Hemley. Crystal structure of a high-pressure/high-temperature phase of alumina by in

situ x-ray diffraction. *Nature Materials*, 3(6):389–393, 2004.

[15] Y. Z. Ma, M. Somayazulu, G. Y. Shen, H. K. Mao, J. F. Shu, and R. J. Hemley. In situ x-ray diffraction studies of iron to earth-core conditions. *Physics of the Earth and Planetary Interiors*, 143-44:455–467, 2004.

[16] H. Mao, W. A. Bassett, and T. Takahashi. Effect of pressure on crystal structure and lattice parameters of iron up to 300 kbar. *Journal of Applied Physics*, 38(1):272–276, 1967.

[17] F. M. Wang and R. Ingalls. Iron bcc-hcp transition: Local structure from x-ray-absorption fine structure. *Physical Review B*, 57(10):5647–5654, 1998.

[18] W. A. Bassett and E. Huang. Mechanism of the body-centered cubic hexagonal close-packed phase-transition in iron. *Science*, 238(4828):780–783, 1987.

[19] a. P. Jephcoat, H. K. Mao, and P. M. Bell. Static compression of iron to 78-gpa with rare-gas solids as pressure-transmitting media. *Journal of Geophysical Research-Solid Earth and Planets*, 91(B5):4677–4684, 1986.

[20] C.S. Smith. *Trans. Metall. Soc. AIME*, 212:574, 1958.

[21] J.W. Forbes. PhD thesis, Washington State University, 1976.

[22] G. E. Duval and R. A. Graham. Phase-transitions under shock-wave loading. *Rev. Mod. Phys.*, 49(3):523–579, 1977.

[23] L. M. Barker and Hollenba.Re. Shock-wave study of alpha reversible epsilon-phase transition in iron. *Journal of Applied Physics*, 45(11):4872–4881, 1974.

[24] T. Sano, H. Mori, E. Ohmura, and I. Miyamoto. Femtosecond laser quenching of the epsilon phase of iron. *Appl. Phys. Lett.*, 83(17):3498–3500, 2003.

[25] K. Kadau, T. C. Germann, P. S. Lomdahl, and B. L. Holian. Microscopic view of structural phase transitions induced by shock waves. *Science*, 296(5573):1681–1684, 2002.

[26] W. G. Burgers. On the process of transition of the cubic-body-centered modification into the hexagonal-close-packed modification of zirconium. *Physica*, 1(7-12):561, 1934.

[27] A. Loveridge-Smith, A. Allen, J. Belak, T. Boehly, A. Hauer, B. Holian, D. Kalantar, G. Kyrala, R. W. Lee, P. Lomdahl, M. A. Meyers, D. Paisley, S. Pollaine, B. Remington, D. C. Swift, S. Weber, and J. S. Wark. Anomalous elastic response of silicon to uniaxial shock compression on nanosecond time scales. *Phys. Rev. Lett.*, 86(11):2349–2352, 2001.

[28] E. M. Bringa, J. U. Cazamias, P. Erhart, J. Stolken, N. Tanushev, B. D. Wirth, R. E. Rudd, and M. J. Caturla. Atomistic shock hugoniot simulation of single-crystal copper. *Journal of*

Applied Physics, 96(7):3793–3799, 2004.

[29] D. M. Beazley and P. S. Lomdahl. Message-passing multicell molecular-dynamics on the connection machine 5. *Parallel Computing*, 20(2):173–195, 1994.

[30] B. L. Holian and P. S. Lomdahl. Plasticity induced by shock waves in nonequilibrium molecular-dynamics simulations. *Science*, 280(5372):2085–2088, 1998.

[31] A.F. Chen S.P. Harrison, R.J. Voter. Embedded atom potential for bcc iron. *Atomistic Simulation of Materials: Beyond Pair Potentials. Proceedings held September 25-30, 1988*, pages 219–222, 1989.

[32] L. M. Barker. Alpha-phase hugoniot of iron. *Journal Of Applied Physics*, 46(6):2544–2547, 1975.

[33] K. Rosolankova. *Picosecond X-ray Diffraction from Shock-Compressed Metals: Experiments and Computational Analysis of Molecular Dynamics Simulations*. PhD thesis, University of Oxford, 2005.

[34] K. Rosolankova, D. H. Kalantar, J. F. Belak, E. M. Bringa, M. J. Caturla, J. Hawreliak, B. L. Holian, K. Kadau, P. S. Lomdahl, T. C. Germann, R. Ravelo, J. Sheppard, and J. S. Wark. X-ray diffraction from shocked crystals: Experiments and predictions of molecular dynamics simulations. volume 706, pages 1195–1198. AIP, 2004.

[35] D. H. Kalantar, E. A. Chandler, J. D. Colvin, R. Lee, B. A. Remington, S. V. Weber, L. G. Wiley, A. Hauer, J. S. Wark, A. Loveridge, B. H. Failor, M. A. Meyers, and G. Ravichandran. Transient x-ray diffraction used to diagnose shock compressed si crystals on the nova laser. *Review of Scientific Instruments*, 70:629–632, 1999.

[36] D.H. Kalantar, E. Bringa, M. Caturla, J. Colvin, K. T. Lorenz, M. Kumar, J. Stolken, A. M. Allen, K. Rosolankova, J. S. Wark, M. A. Meyers, M. Schneider, and T. R. Boehly. Multiple film plane diagnostic for shocked lattice measurements (invited). *Review of Scientific Instruments*, 74:1929–1934, 2003.

[37] D. H. Kalantar, J. Belak, E. Bringa, K. Budil, M. Caturla, J. Colvin, M. Kumar, K. T. Lorenz, R. E. Rudd, J. Stolken, A. M. Allen, K. Rosolankova, J. S. Wark, M. A. Meyers, and M. Schneider. High-pressure, high-strain-rate lattice response of shocked materials. *Physics of Plasmas*, 10(5):1569–1576, 2003.

[38] D. W. Phillion and C. J. Hailey. Brightness and duration of x-ray-line sources irradiated with intense 0.53-mu-m laser-light at 60 and 120 ps pulse width. *Physical Review A*, 34(6):4886–

4896, 1986.

[39] E. A. Kozlov, I. V. Telichko, D. M. Gorbachev, D. G. Pankratov, A. V. Dobromyslov, and N. I. Taluts. The metastability and incompleteness of the alpha-epsilon phase transformation in unalloyed iron loading pulses: Specific features under the effect of threshold of the deformation behavior and structure of armco iron. *Physics of Metals and Metallography*, 99(3):300–313, 2005.

[40] A. D. Ritchie, M. W. Guinan, and Lawrence Livermore National Laboratory. *Evaluation Of Third Order Elastic Constants For Cubic Crystals*. PhD thesis, 1968.

[41] K. Kadau, T. C. Germann, P. S. Lomdahl, and B. L. Holian. Atomistic simulations of shock-induced transformations and their orientation dependence in bcc fe single crystals. *Physical Review B*, 72(6):–, 2005.

[42] B. E. Warren. *X-ray diffraction*. Dover Publications, New York, dover edition, 1990. B.E. Warren. ill.; 22 cm. Reprint. Originally published: Reading, Mass.: Addison-Wesley Pub. Co., 1969. Originally published in series: Addison-Wesley series in metallurgy and materials.

[43] J. Edwards, K. T. Lorenz, B. A. Remington, S. Pollaine, J. Colvin, D. Braun, B. F. Lasinski, D. Reisman, J. M. McNaney, J. A. Greenough, R. Wallace, H. Louis, and D. Kalantar. Laser-driven plasma loader for shockless compression and acceleration of samples in the solid state. *Phys. Rev. Lett.*, 92(7):–, 2004.

[44] K. T. Lorenz, M. J. Edwards, S. G. Glendinning, A. F. Jankowski, J. McNaney, S. M. Pollaine, and B. A. Remington. Accessing ultrahigh-pressure, quasi-isentropic states of matter. *Physics of Plasmas*, 12(5):–, 2005.